

Simulation of a North American Monsoon Gulf Surge Event and Comparison to Observations

ANDREW J. NEWMAN* AND RICHARD H. JOHNSON

Department of Atmospheric Science, Colorado State University, Fort Collins, Colorado

(Manuscript received 18 August 2011, in final form 27 February 2012)

ABSTRACT

Gulf surges are transient disturbances that propagate along the Gulf of California (GoC) from south to north, transporting cool moist air toward the deserts of northwest Mexico and the southwest United States during the North American monsoon. They have been shown to modulate precipitation and have been linked to severe weather and flooding in northern Mexico and the southwest United States. The general features and progression of surge events are well studied, but their detailed evolution is still unclear. To address this, several convection-permitting simulations are performed over the core monsoon region for the 12–14 July 2004 gulf surge event. This surge event occurred during the North American Monsoon Experiment, which allows for extensive comparison to field observations.

A 60-h reference simulation is able to reproduce the surge event, capturing its main characteristics: speed and direction of motion, thermodynamic changes during its passage, and strong northward moisture flux. While the timing of the simulated surge is accurate to within 1–3 h, it is weaker and shallower than observed. This deficiency is likely due to a combination of weaker convection and lack of stratiform precipitation along the western slopes of the Sierra Madre Occidental than observed, hence, weaker precipitation evaporation to aid the surge. Sensitivity simulations show that convective outflow does modulate the intensity of the simulated surge, in agreement with past studies. The removal of gap flows from the Pacific Ocean across the Baja Peninsula into the GoC shows they also impact surge intensity.

1. Introduction

The North American monsoon (NAM) has the typical characteristics of a monsoon: a seasonal wind reversal and areas receiving a significant portion of their annual precipitation during the NAM (Carleton et al. 1990; Badan-Dangon et al. 1991; Douglas et al. 1993; Douglas 1995; Stensrud et al. 1995; Adams and Comrie 1997; Anderson et al. 2000a; Vera et al. 2006; Johnson et al. 2007). Regions in the core of the monsoon (northwest Mexico) receive up to 80% of their annual rainfall during the NAM season (Douglas et al. 1993). This

makes the NAM critical to regional water resource management and agriculture practices.

The North American Monsoon Experiment (NAME) field campaign (Higgins et al. 2006) produced an unprecedented set of in situ and remotely sensed observations of the core NAM region, mainly in the Sinaloa and Sonora provinces and the Gulf of California (GoC; Fig. 1). The NAME dataset includes surface and upper-air observations, vertical wind profiling radar, the National Center for Atmospheric Research (NCAR) polarimetric radar (S-Pol) along with two Mexican radars, aircraft, and many other observational platforms (Higgins et al. 2006). Most instruments were in place from 1 July–15 August with two strong gulf surge events observed, 12–14 July and 22–24 July 2004, the first of which is the subject of this study.

Knowledge of features modulating NAM precipitation is essential to fully understand core NAM rainfall characteristics. One such feature is the gulf surge event, or surge event for short. These transient episodes have been tied to moisture flux and precipitation anomalies during the NAM (Anderson et al. 2000b; Berbery 2001;

* Current affiliation: National Center for Atmospheric Research, [†]Boulder, Colorado.

[†] The National Center for Atmospheric Research is sponsored by the National Science Foundation.

Corresponding author address: Andrew Newman, National Center for Atmospheric Research, Boulder, CO 80307.
E-mail: anewman@ucar.edu

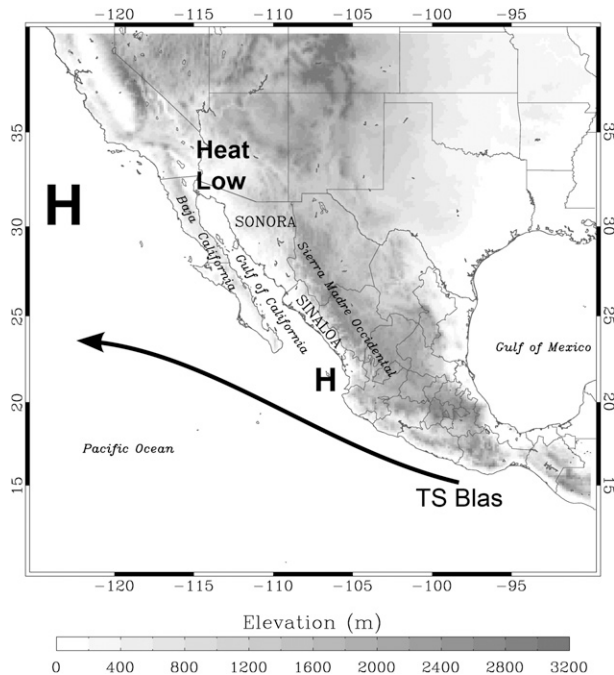


FIG. 1. Overview of the NAM region during the 12–14 Jul 2004 surge event. Geographic and political boundaries are noted. The black line indicates the general path of Tropical Storm Blas, “heat low” indicates the position of surface heat low in the desert Southwest, while the two surface high pressure centers are indicated by H.

Douglas and Leal 2003; Gochis et al. 2004; Higgins et al. 2004; Douglas and Englehart 2007) and severe weather outbreaks in Arizona (Maddox et al. 1995). Hales (1972) and Brenner (1974) first introduced the concept of a “surge” of near-surface cool, moist air providing moisture to the monsoon region from the tropical east Pacific channeled through the GoC by the Sierra Madre Occidental (SMO) and Baja California Peninsular Ranges (Fig. 1). The general characteristics of surge events have since been well studied (Hales 1972; Brenner 1974; Badan-Dangon et al. 1991; Anderson et al. 2000b; Douglas and Leal 2003; Bordoni and Stevens 2006), while other work has linked surge events to tropical easterly wave (TEW) or tropical cyclone (TC) passages south of the GoC (Hales 1972; Brenner 1974; Stensrud et al. 1997; Fuller and Stensrud 2000; Higgins and Shi 2005; Johnson et al. 2007; Adams and Stensrud 2007). Finally, there have been several modeling and observational studies that have examined surge evolution (Stensrud et al. 1997; Rogers and Johnson 2007, hereafter RJ07; Adams and Stensrud 2007; Mejia et al. 2010). However, these studies have either been exclusively observational (RJ07; Mejia et al. 2010), leaving out significant portions of time/area in their analyses, or use

a model grid spacing that required the use of a convective parameterization (Stensrud et al. 1997; Adams and Stensrud 2007).

The main goal of this work is to combine the vast array of observations of NAME with a model simulation that uses horizontal and vertical grid spacing sufficient to explicitly resolve convective systems.¹ This approach will provide a detailed view of the evolution of a surge event from the model perspective while comparing with observations to explore model performance. By examining a surge event within a high-resolution framework, this paper 1) assesses the capabilities of the Weather Research and Forecasting Model (WRF) to simulate an event, and 2) extends past observational and modeling studies of surge events. The observational data used and model configurations are stated in the next two sections, followed by the detailed examination of the base model simulation and comparisons to the multitude of NAME observations along with discussion of two sensitivity simulations. Last, some concluding remarks and a general overview of the simulated surge evolution are discussed.

2. NAME observations

a. Integrated sounding system

Three integrated sounding systems (ISSs) were deployed from 7 July to 15 August at Puerto Penasco (PP), Kino Bay (KB), and Los Mochis (LM; Fig. 2). These systems are maintained by NCAR and contain a bevy of instrumentation including a surface station measuring temperature, pressure, relative humidity, wind speed, and direction at 1-min intervals; a global positioning system rawinsonde sounding system measuring temperature, pressure, relative humidity, and wind speed/direction; a 915-MHz Doppler clear-air wind profiler (915-MHz profiler hereafter) measuring vertical profiles of wind speed/direction; and a radio acoustic sounding system (RASS) measuring vertical profiles of virtual potential temperature. Data are subject to quality control via NCAR-developed algorithms and human inspection (RJ07). The reader is referred to RJ07 for details concerning quality control of the ISS data. Model surface variables, wind profile time series, and atmospheric soundings will be compared to the ISS data to give comparisons of the surface and vertical evolution of the surge event.

¹ The horizontal resolution (4 km) is insufficient to resolve individual convective clouds, but permits gridscale convection without a convective parameterization. See section 3 for more discussion.

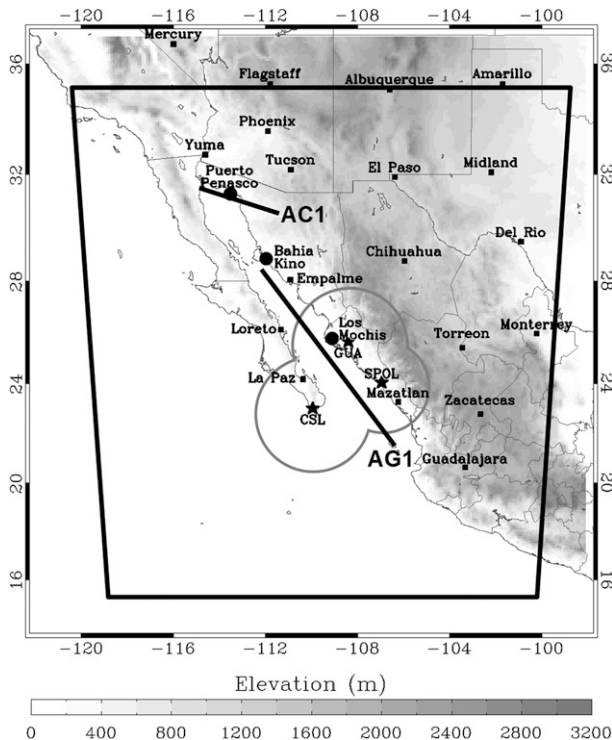


FIG. 2. General core NAM region with the model domain outlined (trapezoid). Also depicted are the three ISS sites (large circles): Puerto Penasco (PP), Kino Bay (KB), and Los Mochis (LM) as well as the radar sites (stars): Cabo San Lucas (CSL), Guasave (GUA), and the NCAR S-Pol (S-Pol) with the gray rings denoting the approximate range of the three radars. AG1 and AC1 denote the along-gulf and across-gulf cross sections the NOAA WP-3D performed on 12 and 13 July, respectively.

b. Aircraft observations

During intensive observing periods (IOPs) a National Oceanic and Atmospheric Administration (NOAA) WP-3D aircraft was flown to sample the low-level structure of gulf surge events (Mejia and Douglas 2005) with temperature and wind speed/direction measurements at flight level with 1-s resolution. During the 12–14 July surge event two flights were made: one on 12 July and one on 13 July. These data are examined in detail by Mejia et al. (2010) and provide vertical cross sections showing the low-level structure of the GoC 12 h prior to surge initiation and of the surge in the northern GoC, respectively. Model cross sections along the flight path will be compared to the flight cross sections to assess the three-dimensional simulated surge structure.

c. Radar network

The radar network dataset is a gridded dataset comprising NCAR S-band polarimetric radar (S-Pol) and two Servicio Meteorológico Nacional (SMN) Doppler radars with 2-km horizontal and 15-min temporal

resolution (Lang et al. 2007). The network is located in the southern NAM region near the mouth of the GoC (Fig. 2). Reflectivity from this network will be used as validation data against model-simulated reflectivity of convection in association with the surge event. Qualitative comparisons at critical junctures on 12 and 13 July will give insight into the simulated convective evolution and help to highlight reasons for discrepancies between the simulation and observed surge. Quantitative comparisons of reflectivity are not performed in this study because of the pitfalls of comparing observed and simulated reflectivity. First, assumptions about the size distributions present in precipitation are made to arrive at a simulated reflectivity, which may give rise to substantial errors (e.g., Marshall and Palmer 1948; Jones 1956). Second, radar and model grid differences would introduce interpolation errors. However, qualitative comparisons of reflectivity intensity and quantitative comparisons of coverage area (grid points >0 dBZ in observed and simulated reflectivity fields) are used to demonstrate the ability of the model to reproduce convection at the appropriate spatial and temporal locations.

3. Model configuration

The Advanced Research core (ARW) of the Weather Research and Forecasting Model (WRF) version 3.2.1 was used for all simulations. Only one high-resolution domain was used, which removes possible numerical errors, complexities, and uncertainties associated with nested grids and convective parameterizations (Pielke 2002; Stensrud 2007; Warner 2011). The horizontal domain is $2000 \text{ km} \times 2320 \text{ km}$ (Fig. 2) with a horizontal grid spacing of 4 km (501×581 grid points). The vertical grid, composed of 55 levels between the surface and 100 hPa, is stretched from 7 levels in the lowest 1 km to a maximum Δz of ~ 340 m near the model top to emphasize boundary layer features. The Rapid Radiative Transfer Model longwave, Dudhia shortwave, Thompson et al. (2008) microphysics (with bug fixes), Noah land surface model, and Quasi-Normal Scale Elimination (QNSE) surface and boundary layer schemes are used for all simulations. The North American Regional Reanalysis (NARR) is used for all initial and boundary conditions. NARR data are produced 8 times daily (3-h interval) and contain 29 vertical levels from 1000 to 100 hPa at 32-km horizontal grid spacing (Mesinger et al. 2006). All simulations are initialized at 1200 UTC 11 July and integrated until 0000 UTC 14 July. Analysis begins at 0600 UTC 12 July, providing 18 h of spinup time for WRF to generate the appropriate smaller-scale circulations and precipitation features.

Sensitivity simulations (not shown) on model domain location within the NAME region and on vertical levels were performed to obtain a domain that best reproduces the observed phenomena. It was found that the domain needed to be large enough to capture Tropical Storm (TS) Blas (Fig. 1), the entirety of the SMO and Baja ranges, and at least a portion of the southwest U.S. heat low. Additionally, it was found that a minimum of 50 vertical levels were required to properly simulate convective initiation. The explanation may lie in weak boundary layer vertical velocities ($\sim 10 \text{ cm s}^{-1}$) near convective initiation. This may cause simulations with lower vertical resolution to improperly terminate incipient updrafts due to an overly strong capping inversion, via the NARR initial conditions, combined with the weak updrafts (similarly to that in Barthlott et al. 2010). However, this has not been pursued further as the exploration into the causes of the vertical sensitivity is outside the scope of this work.

It is recognized that 4-km grid spacing is not adequate to fully resolve convection (Bryan et al. 2003; Bryan and Morrison 2012); however, it is sufficient to resolve the circulations and motions most pertinent to the gulf surge event. To approach true convection-resolving simulations ($\sim 1\text{-km}$ horizontal grid spacing; Bryan and Morrison 2012) approximately 64 times the computational resources required for the 4-km simulation is required, which was not possible given that multiple simulations were performed. A portion of the control simulation was performed at 2-km horizontal resolution and the evolution of the initial convection on 12 July is similar in most regards. The 2-km simulation (not shown) has slightly more stratiform precipitation, smaller convective cores, and stronger updrafts in agreement with Bryan and Morrison (2012). Li et al. (2008) demonstrated convection-permitting grid spacing (3 km) to be capable of resolving NAM processes and Weisman et al. (2011, manuscript submitted to *Mon. Wea. Rev.*) successfully simulated an MCS using similar grid spacing. While the smoothing and weakening of convective gust fronts and convective updrafts are likely (Bryan and Morrison 2012), the evolution of the surge event should not be qualitatively altered by a slightly coarser horizontal resolution.

Two modifications to the control run were made and are compared to it in order to evaluate the impacts these modifications have on surge evolution. The first modified run eliminates below-cloud evaporation to assess how altered convective outflows affect surge initiation. The second modification is to raise the height of the Baja California Mountains, which will test the role of gap flows through the peninsular ranges in surge evolution.

a. Evaporation modification

To examine the influence of convective outflows on surge evolution, a modification to the Thompson microphysics scheme was made to remove below-cloud evaporation. Cloud base is computed at each grid point by determining the lowest level having a cloud water mixing ratio above 0.1 g kg^{-1} , near the edge of the visual cloud extent (Warner 1969). No rain or cloud water evaporation is allowed to take place below that level (typically $\sim 775\text{--}825 \text{ hPa}$ in convective cores, $\sim 625\text{--}675 \text{ hPa}$ in stratiform areas). This is a less intrusive way to modify the microphysics of convection than removing all cooling tendencies or ice microphysics (e.g., Gilmore et al. 2004; Trier et al. 2011) yet still substantially modify the mechanisms of convective outflow generation. The selective removal of below-cloud evaporation still allows for outflow generation via precipitation loading, melting ice, and evaporatively cooled air originating above the cloud base. However, the cold pools created are weaker than when below-cloud evaporation is allowed (see section 5).

b. Filled peninsular ranges

The peninsular ranges (Fig. 1) extend along the length of the peninsula with many peaks and low spots creating a barrier having many gaps open to the Pacific Ocean, allowing flows into the GoC from the North Pacific (Anderson et al. 2001; Bordoni et al. 2004). This influx of cool, dense air into the central and northern GoC is hypothesized to influence the evolution of the surge event through two possible mechanisms. The first is that cool dense air helps reinforce lower-atmosphere stratification present in the GoC, helping to create an environment conducive to propagating features such as internal bores. The second is that the Pacific air modifies conditions along the eastern coast of the GoC, weakening convection in the region. Weaker convection would lead to less convective outflow and a weaker initial surge event. To test these possible mechanisms, the topography along the peninsular ranges is modified by setting all points along the peninsula from the southern end to 31.5°N to 1000 m in order to create a continuous barrier along the peninsula. North of 31.5°N the peninsular ranges are continuously above $\sim 900 \text{ m}$ in elevation. This modification will block nearly all flow into the GoC from the Pacific Ocean. Comparisons between the modified topography run and the control run will be presented to highlight the importance of these mechanisms in surge evolution.

4. Surge evolution

RJ07 gives an in-depth overview of the actual surge evolution, so it will not be discussed in detail here.

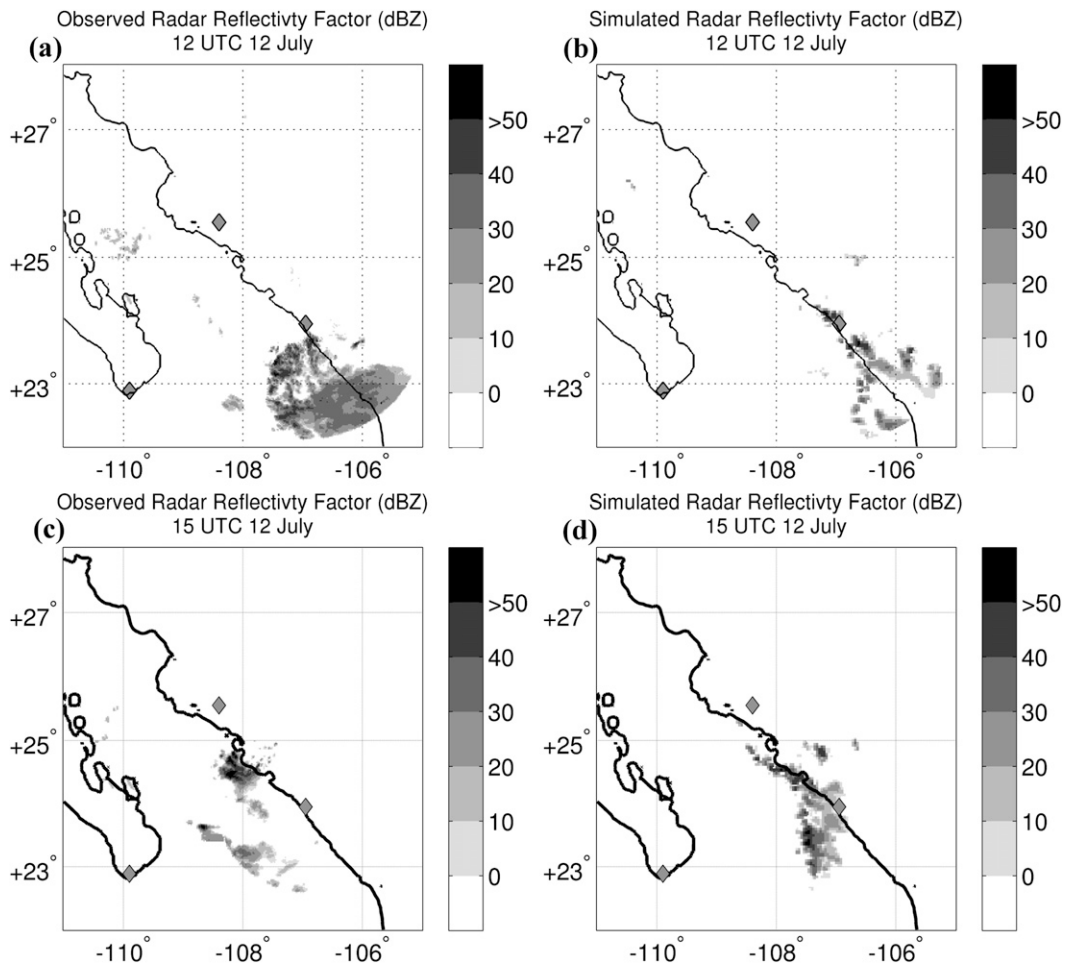


FIG. 3. (a),(c) Observed radar reflectivity and (b),(d) model-derived radar reflectivity using the WRF post processor. (a),(b) At 1200 UTC 12 Jul; (c),(d) at 1500 UTC 12 Jul. The gray diamonds denote the three radar sites.

However, some important features to note are the TEW that develops into TS Blas, passing near the mouth of the GoC (Figs. 2 and 3; RJ07) and two convective events. The first, a convective cluster, forms around 0600 UTC 12 July near the mouth of the GoC and moves into the GoC around 1200 UTC 12 July (Fig. 3a). This convective cluster is associated with the TEW and the formation of TS Blas. The second, diurnal convection along the central and northern SMO, develops after 1800 UTC 12 July (not shown), is near its greatest extent around 0300 UTC 13 July, and dissipates by 1200 UTC 13 July. This convection produces multiple convective outflows over several areas, some of which are noted in the following discussion when relevant to model performance and their involvement in the initial surge event on 13 July.

a. Precursor disturbance, 12 July

The convective cluster in the southern GoC at 1200 UTC (Figs. 3a,c) (associated with the TEW precursor

to TS Blas) has a well-defined leading arc of convection with a trailing stratiform region and a likewise well-defined cold pool, as indicated by aircraft observations (Mejia et al. 2010). Convection in the simulation is not as well organized with the leading convection being more of a broken line with much less trailing stratiform precipitation. The simulation places the cluster 130 km southeast of the real location and has a precipitation area 35% smaller than the observable portion (Fig. 3b). At 1500 UTC the simulation reproduces the small convective cluster near the coast reasonably well (Figs. 3c,d). The observed precipitation area is 17% greater in the simulation at 1500 UTC. Furthermore, the motion of the simulated convection is slightly slower ($1\text{--}3\text{ m s}^{-1}$) than observed between 1200–1500 UTC, which would agree with a weaker simulated cold pool assuming the vorticity balance theory put forth in Rotunno et al. (1988) explains the maintenance and dynamics of the cluster, while the gravity current theory explains the motion of the cluster (Benjamin 1968). The

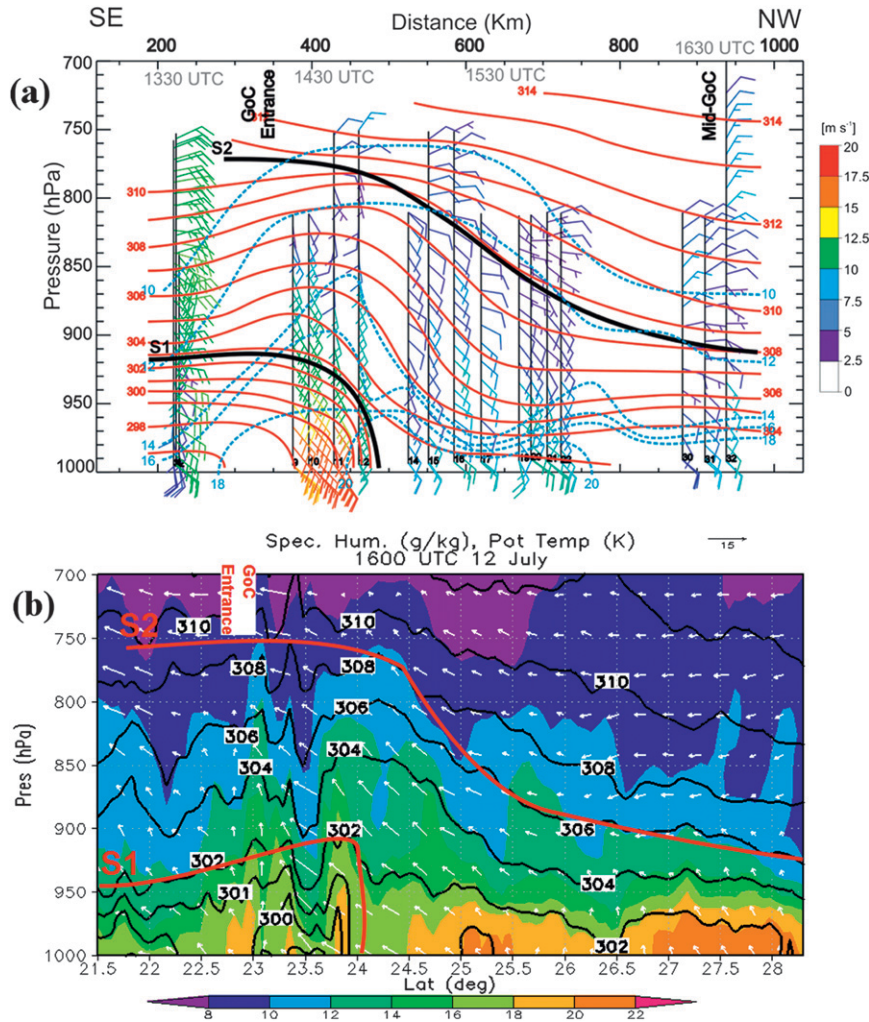


FIG. 4. Along-gulf (AG1) cross section (CS) (Fig. 2) (a) from the NOAA WP-3D adapted from Mejia et al. (2010) and (b) from the control simulation. WP-3D CS runs from ~1300–1700 UTC, simulated CS taken at 1600 UTC. Potential temperature (orange lines) and mixing ratio (blue dashed lines) contoured and wind barbs color coded by wind speed are shown in (a). Potential temperature (black lines) contoured and mixing ratio (shading) and wind vectors (arrows) are shown in (b). S1 denotes cold pool associated with convection near GoC entrance and S2 denotes the deeper disturbance discussed in Mejia et al. (2010). Black lines in (a) and red lines in (b) give general boundaries of S1 and S2, respectively.

relatively coarse model grid spacing may contribute to the weaker convection via reduced updraft vertical velocities and cold pool gradients (Bryan and Morrison 2012).

Figure 4 displays a cross section (CS) of wind and potential temperature from the NOAA WD-P3 aircraft (Mejia et al. 2010) (Fig. 4a) and the simulation (Fig. 4b) with the cold pool moving from left right (south to north). The model CS is along nearly the same line as reality (AG1; Fig. 2), with the northern point being nearly identical, but the southern point being shifted about 80 km farther east (toward the coast) in response to the simulated convection placement (Figs. 3a,b). The

model cold pool has a minimum potential temperature of around 299 K while the actual minimum is near 297 K. Also, the actual cold pool is slightly more moist, ~30 hPa deeper, and has substantially stronger winds. The simulated cold pool has features consistent to that of a gravity current: temperature decreases, wind speed increases and direction changes, and surface pressure increases with the passage of the cold pool (Simpson 1982; Haertel et al. 2001), in agreement with Mejia et al. (2010). Mejia et al. (2010) label the cold pool as structure 1 (S1) and that designation will be used herein. The red line in Fig. 4b denoting S1 was drawn subjectively

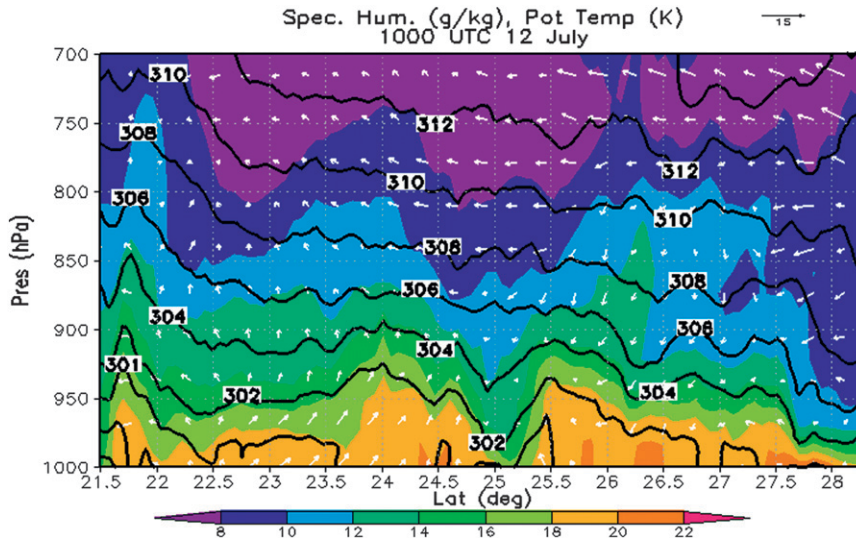


FIG. 5. As in Fig. 4b, but at 1000 UTC 12 Jul.

using wind speed/direction changes and potential temperature gradients to locate the leading edge.

Although the control run cold pool is warmer and has less intense winds, it is still able to generate a deeper response reflected as an undulation of the isentropes about 100 km ahead of the cold pool leading edge (Fig. 4b). It is believed that the leading feature is generated by S1 because it is not present in the southern GoC prior to the convective cluster moving into the region (Fig. 5). This feature is real and is noted as structure 2 (S2) by Mejia et al. (2010) and in this work. Ahead of S2 (near 27.5°N in Fig. 4b) the 12 g kg⁻¹ mixing ratio line is near 925 hPa, and behind S2 it is located near 825 hPa. There is an increase in wind speed and a change in wind direction behind the leading edge of S2, along with essentially no decrease in surface temperature and an increase in surface pressure (not shown), which is indicative of a bore or solitary wave passage (Simpson 1997; Knupp 2006). The S2 is likely generated by S1 impinging on the mean state in the southern GoC, which is described by Johnson et al. (2007). Their Fig. 12 shows that the mean state along the GoC is very similar to that of Fig. 4b without convection. The mean state along the GoC has a cold dome over the southern GoC with downward-sloping isentropes toward the heat low over the desert Southwest. Also, the lower levels are relatively stable and can have a low-level inversion present (Douglas et al. 1998; RJ07; Martin and Johnson 2008), which allows for features such as bores or solitary waves to form and propagate. A thorough dynamical analysis of S2 is outside the scope of this paper.

Figure 6 shows model and actual potential temperature and mixing ratio profiles from 1000 to 700 hPa at

LM before and after the passage of S2. As S2 moves up the GoC, slight cooling (above ~975 hPa) and moistening through about 800 hPa occurs in the simulation behind the leading edge. The feature loses definition and becomes washed out near Empalme, Sonora, around 2230 UTC 12 July in the simulation (not shown). Although it appears this feature is not the actual gulf surge signature, it is important because it ushers in a southerly flow regime throughout the southern and central GoC. It also begins to redistribute the cool air from the mouth of the GoC northward. The simulation produces deeper cooling but moistening only through

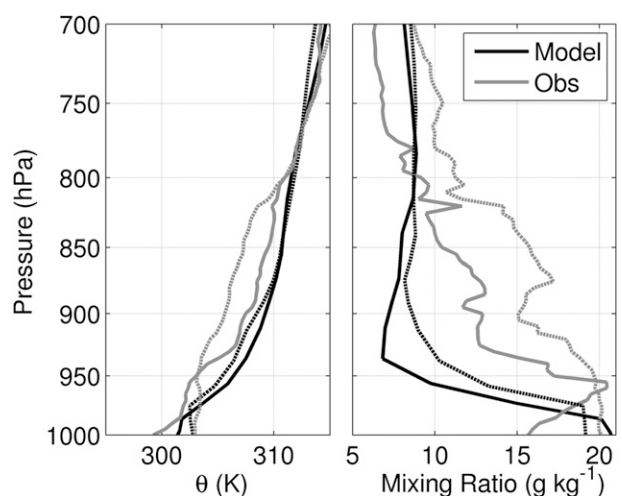


FIG. 6. (left) Potential temperature and (right) mixing ratio at Los Mochis at 1200 (solid) and 1800 (dashed) UTC 12 Jul. The 1200 UTC sounding occurred before the passage of S2 and the 1800 UTC sounding after.

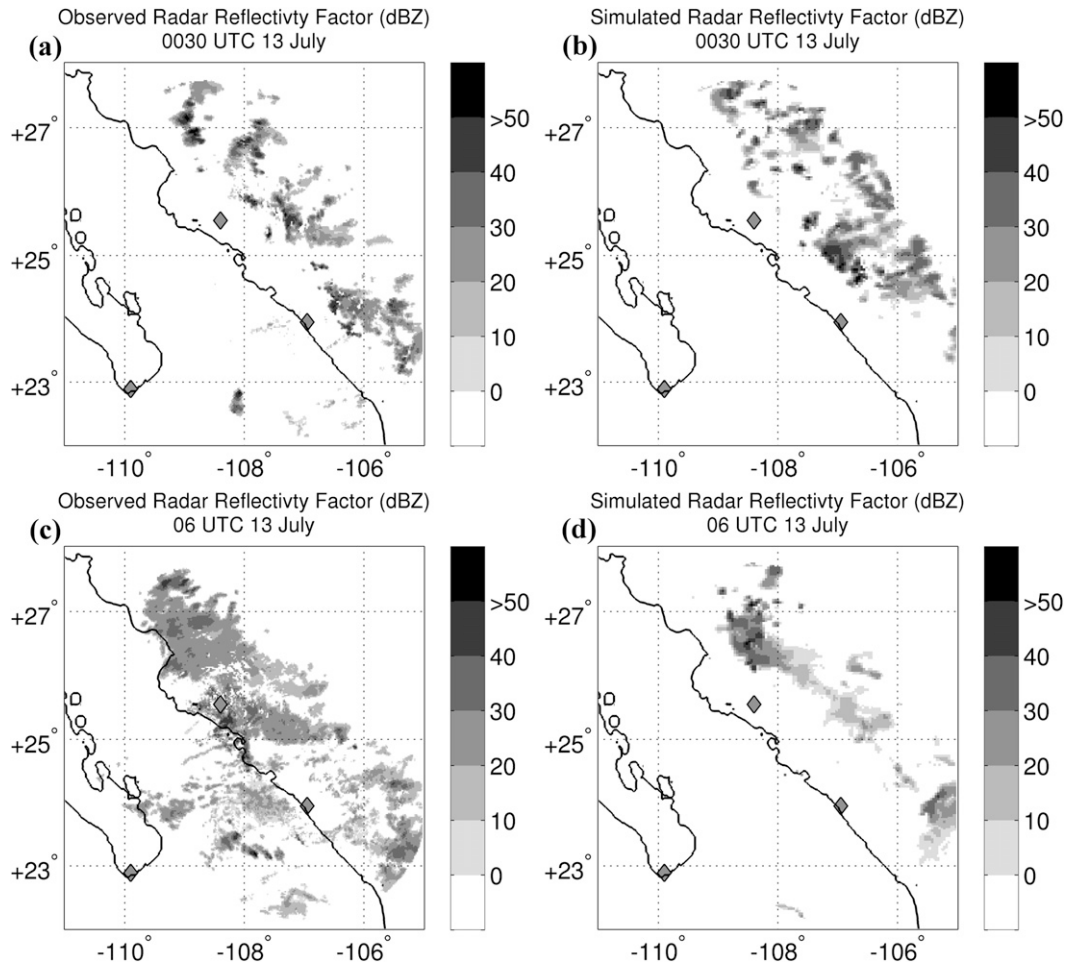


FIG. 7. (a),(c) Observed radar reflectivity and (b),(d) model-derived radar reflectivity using the WRF postprocessor at (top) 0030 UTC 13 Jul and (bottom) 0600 UTC 13 Jul.

820 hPa, and has the largest discrepancies in the boundary layer.

b. Development of surge, 13 July

This section examines the development and motion of the initial surge event on 13 July. At 0030 UTC, the model convection (Fig. 7b) near the southern GoC is organized into several clusters and is moving off the SMO. The real and model convective clusters are in very similar locations at 0030 UTC (Figs. 7a,b). In regards to precipitation coverage area, the radar network actually observes 11% less areal coverage than the control run. However, the simulation produces significantly less convection and stratiform precipitation at 0600 UTC than in reality (Figs. 7c,d). The actual precipitation coverage area is nearly 2.6 times the control run. The main reasons are that the control run convection evolves more rapidly and does not produce enough residual light precipitation. As an example, the model convective cluster

near 24°N dissipates well before 0600 UTC, while the actual cluster is active through 0600 UTC and moves west-northwest to the intersection of 26°N and the coastline (Figs. 7c,d). A faster evolution rate is found in the northern GoC convection as well. Li et al. (2008) show similar results for convective evolution in a 3-km simulation over the same region and Trier et al. (2011) show an enhanced evolution rate and motion for a mid-latitude squall system. Li et al. (2008) show the model overestimates precipitation during the 1800–0600 UTC timeframe and underestimates it from 0600–1200 UTC, which indicates that the initiation and evolution of precipitation occurs too fast in the model.

Model top-of-the-atmosphere and the *Geostationary Operational Environmental Satellite-12* (GOES-12) IR channel brightness temperatures at 0000 and 1200 UTC are shown in Fig. 8. Comparisons highlight that convection and associated high cloudiness are less extensive along the entire SMO in the simulation than in the observations at

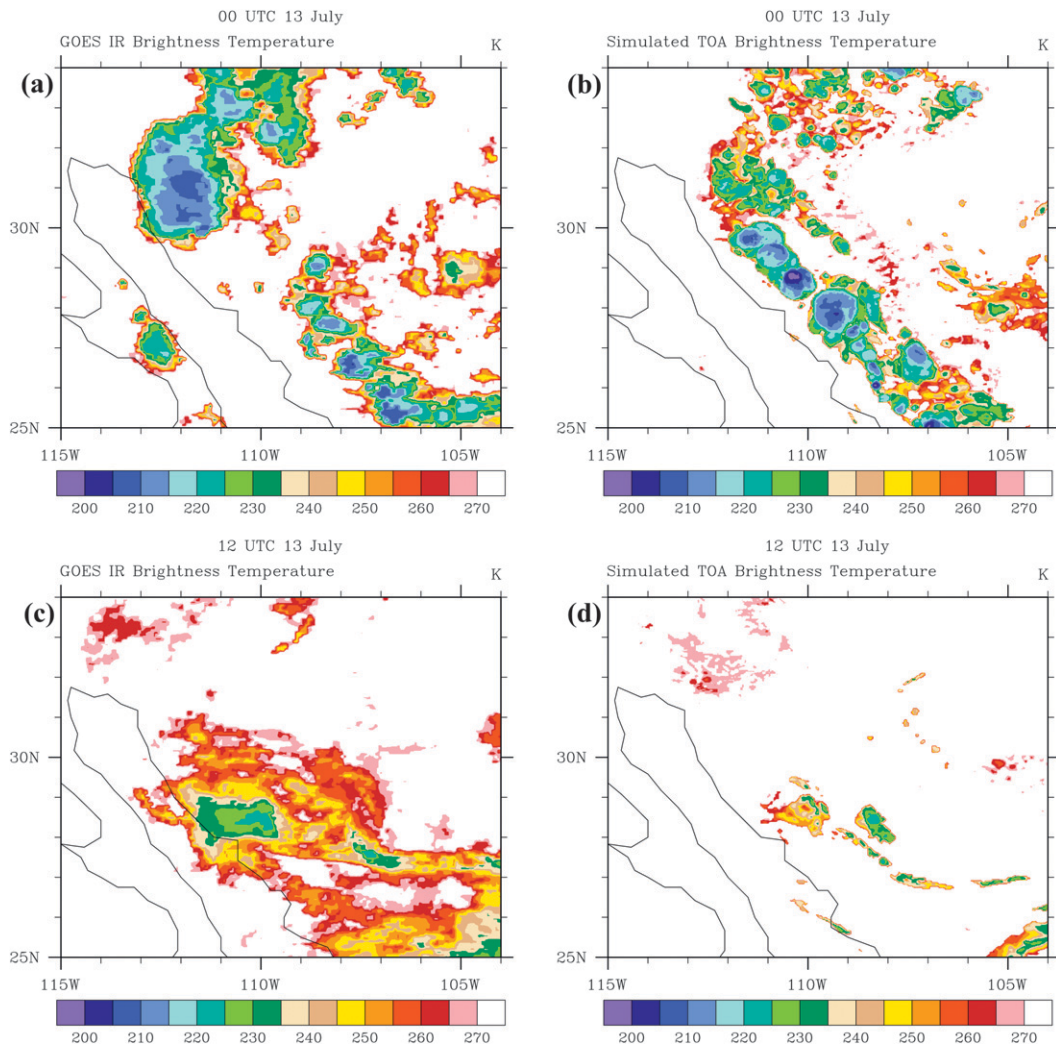


FIG. 8. (a),(c) *GOES-12* IR channel and (b),(d) simulated top-of-the-atmosphere (TOA) brightness temperatures for (top) 0000 and (bottom) 1200 UTC 13 Jul.

0000 UTC. At 0000 UTC, there is $\sim 40\%$ more cloud cover < 260 K in reality than in the simulation. The maturing convective cluster present in the simulation at 0000 UTC near 29°N does not develop in reality until after 0000 UTC (Figs. 8a,b). However, by 1200 UTC nearly all residual convective cloud cover has dissipated in the simulation, while there is still extensive residual cloud cover present in reality (Figs. 8c,d). At 1200 UTC, there is ~ 7 times more cloud cover < 260 K observed than in the simulation. Fortunately, simulating residual convective cloud cover is not critical to surge evolution in this case. However, the amount of stratiform precipitation (less in this case) and rate of convective evolution (faster in this case) are important factors to consider when examining the model surge evolution.

The control run surge initiates in the southern GoC between 0100–0400 UTC 13 July as indicated by the 950-hPa

moisture flux (not shown). At 0400 UTC (Fig. 9a) an area of enhanced moisture flux between 22° and 26.5°N can be seen and is the initial simulated surge beginning to propagate up the GoC. The simulated surge initiates through a combination of 1) an increase in the flux of cool moist air from near the GoC entrance, and 2) air from the west side of the peninsula through the large gap in the southern portion of the peninsular ranges between 23.5° and 25.5°N . By 0800 UTC (Fig. 9b) convective outflow has been impinging on the GoC along the coastline from 27° to 29°N for 2–3 h, complicating the interpretation of where the surge front is located. The most important observation is that the convective outflow appreciably strengthens the surge and can be seen through the large increase in moisture flux values greater than $150 \text{ g m}^{-1} \text{ s}^{-1}$ between 0400 and 0800 UTC. Further complicating matters is the GoC low-level jet

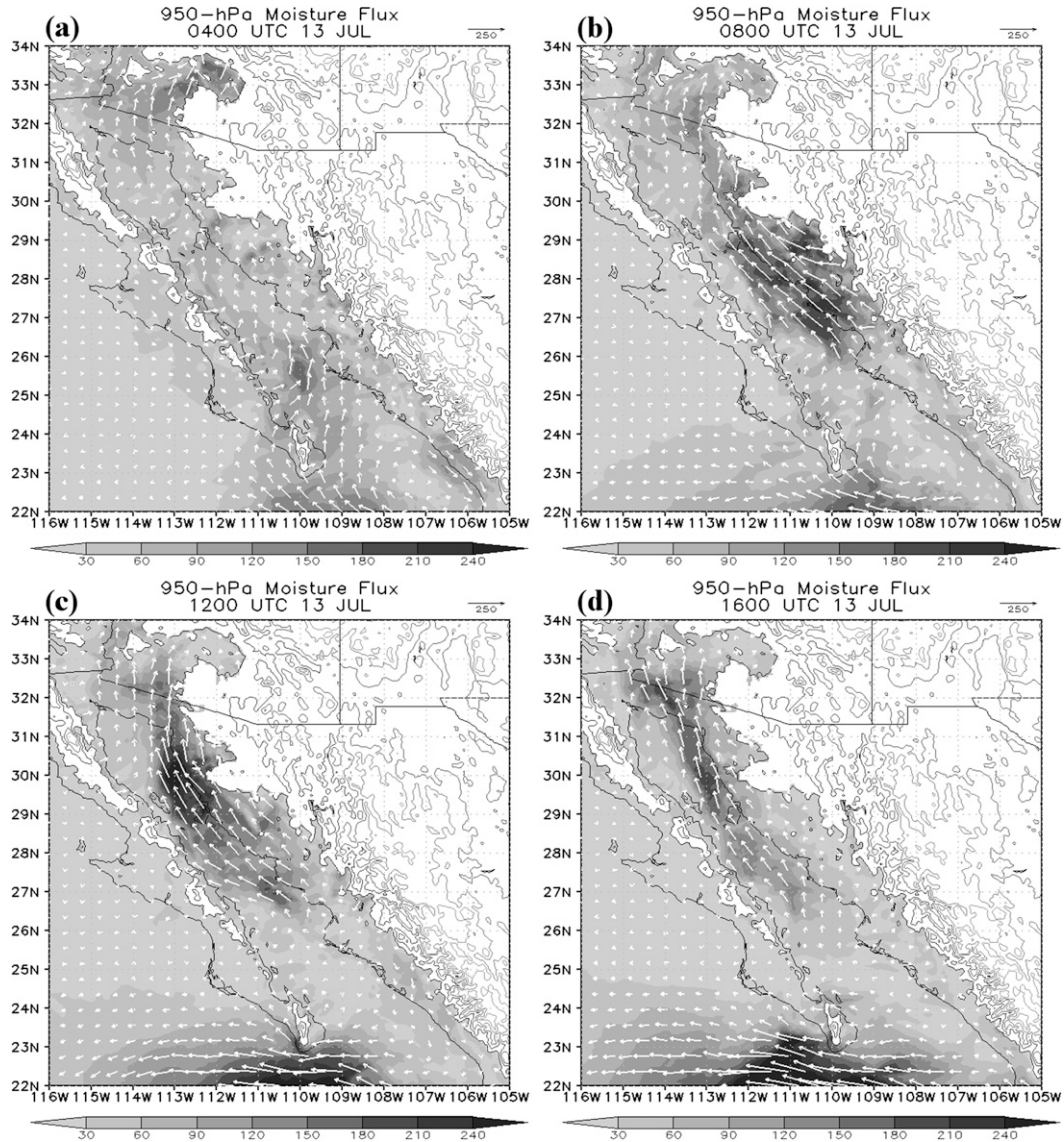


FIG. 9. 950-hPa moisture flux ($\text{g m kg}^{-1} \text{s}^{-1}$) at (a) 0400, (b) 0800, (c) 1200, and (d) 1600 UTC 13 Jul. Light to dark shading corresponds with weak to intense moisture flux.

(LLJ), which climatologically begins to strengthen between 0400–0900 UTC (Douglas et al. 1998; Anderson et al. 2001) at PP. It is manifesting itself as the simulated streamer of enhanced moisture flux ahead of the surge along the east coast of the GoC at 0800 UTC (30° – 33°N , along the GoC coastline). At 1200 UTC (Fig. 9c), the leading edge of the model surge is reaching the northern GoC, and by 1600 UTC (Fig. 9d) the model surge is weakening and spreading out over the desert Southwest. Following the leading edge of the intense moisture flux ($>150 \text{ g m kg}^{-1} \text{ s}^{-1}$) along the GoC between 0400 and 1400 UTC, gives a distance traveled of about 800 km in 10 h, or an average total system speed (intrinsic phase

speed plus background flow) of $\sim 22 \pm 1.5 \text{ m s}^{-1}$ using a total position error of 50 km for the uncertainty estimate. If the central location of the intense moisture flux is used to track the surge (between 0400–1200 UTC, Figs. 9a,c), the surge has a motion of $\sim 19 \pm 2 \text{ m s}^{-1}$. The actual surge is estimated to move at an average total system speed of 17 – 25 m s^{-1} (RJ07).

Shortly after the actual surge wind maximum reached PP, the WP-3D made an across the gulf transect (Fig. 10a), along the line AC1 in Fig. 2. A maximum in actual wind speed just over 20 m s^{-1} near 970 hPa is seen over the east-central GoC, while the 10 m s^{-1} wind contour extends upward to $\sim 890 \text{ hPa}$, westward to Baja California,

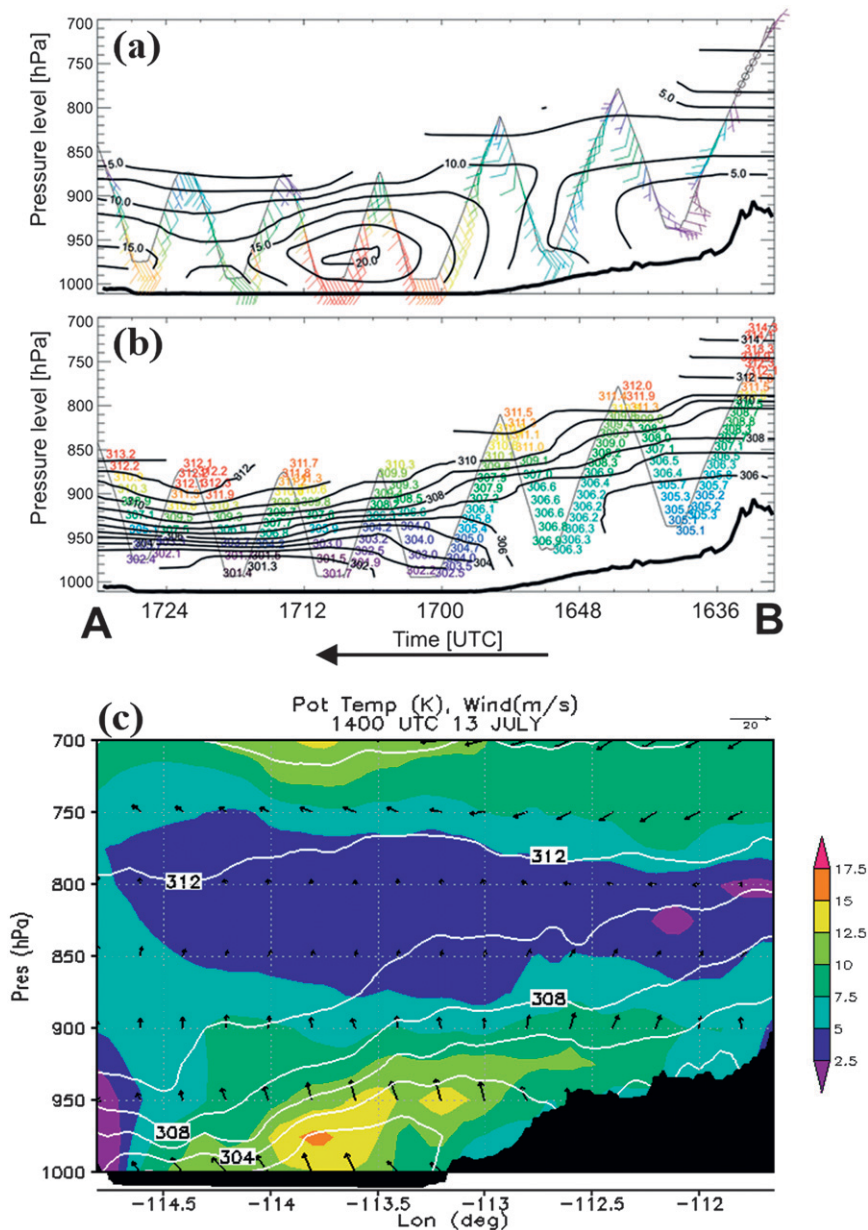


FIG. 10. (a) The observed wind speeds (contours) and barbs (color coded by speed); (b) potential temperature (contours); and (c) modeled wind speed (shading), direction (arrows), and potential temperature (contours). The thick black line in (a),(b) and the black shading in (c) all indicate topography. All panels are along AC1 (Fig. 2). Both (a) and (b) are adapted from Mejia et al. (2010).

and eastward over the coastal plain. There is also a band of greater than 7.5 m s^{-1} southerly winds extending over the ridge along the eastern side of the CS around 900–870 hPa. The model surge is less intense and slightly shallower than observed; it has a maximum wind speed of around 15 m s^{-1} at 975 hPa in the east-central GoC (Fig. 10c). However, the structure of the surge is very similar to that observed with greater than 7.5 m s^{-1}

southerly winds extending above the topography to the east and nearly to the Baja Peninsula in the west. The actual and model surges have a similar potential temperature structure as well (Figs. 10b,c), with the simulation being cooler over the eastern landmass due to it being 3 h earlier (1400 UTC is near local sunrise).

Figures 11a and 12a display model (solid lines) and actual (dotted lines) surface traces of temperature,

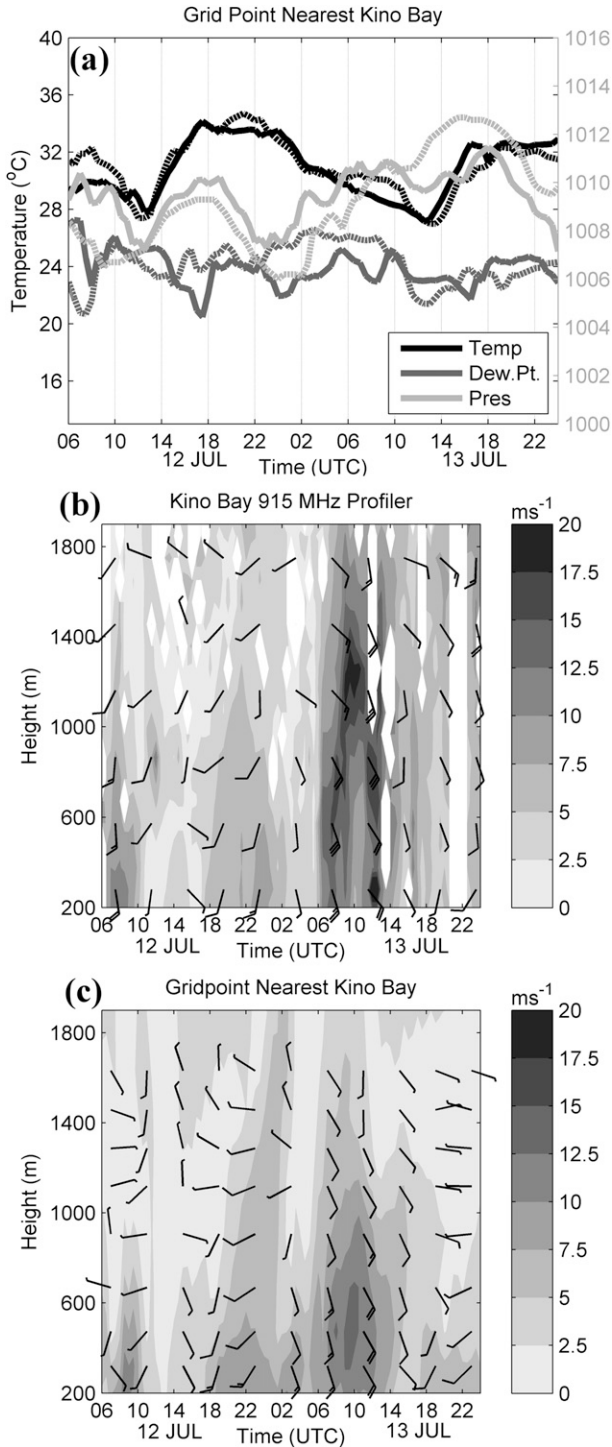


FIG. 11. Time series of surface temperature, dewpoint, and MSLP at Kino Bay for (a) the simulation (solid) and observations (dashed), and (b) the observed and (c) simulated wind profile time series from 0600 UTC 12 Jul–0000 UTC 14 Jul. Barbs in (b) and (c) indicate speed with full barb equal to 5 m s^{-1} and half barb equal to 2.5 m s^{-1} .

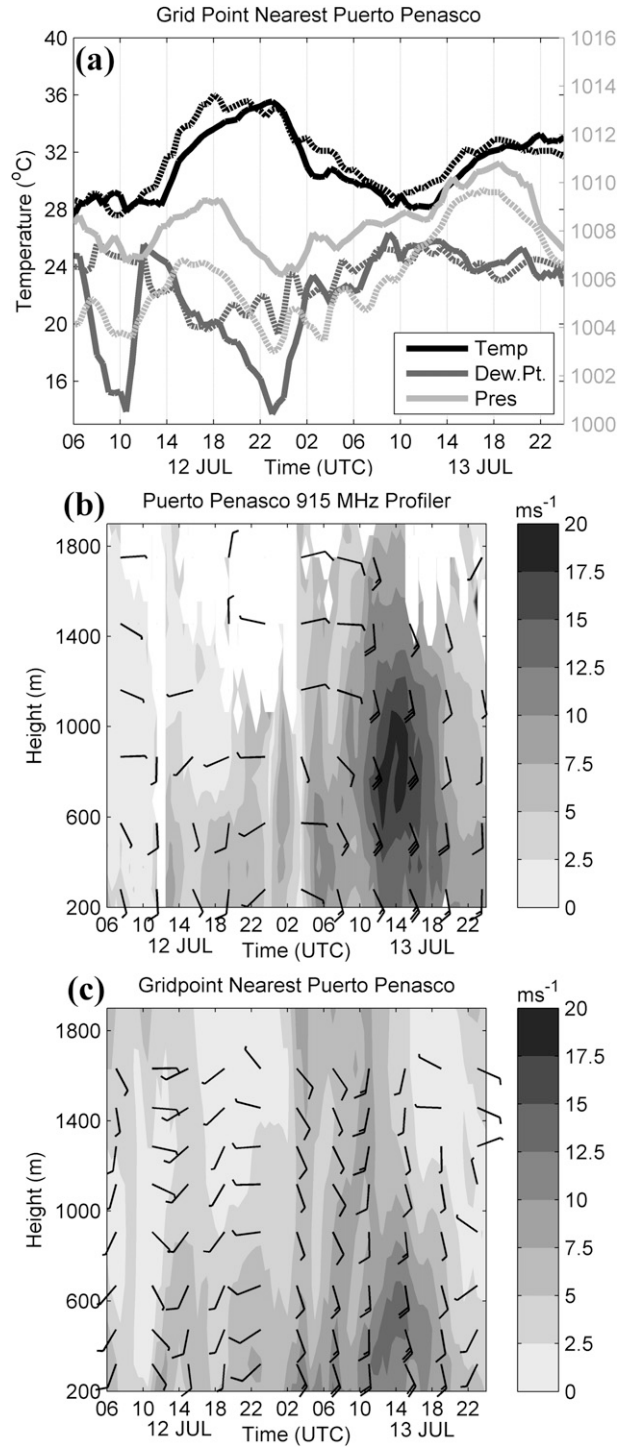


FIG. 12. As in Fig. 11, but for Puerto Penasco.

dewpoint, and mean sea level pressure (MSLP) for KB and PP, while Figs. 11b,c and 12b,c show the actual and model wind profiles respectively, from 200 m to 2 km. At KB, the general diurnal cycle of 2-m temperature and pressure is recreated well and with minimal bias

[root-mean-square error (RMSE)] in MSLP of 0.3 hPa (1.5 hPa), -0.1 K (1.0 K) for temperature, and -0.3 K (2.0 K) for dewpoint. In regard to features of the surge at KB, the simulation reproduces the pressure rise around 0000–0200 UTC 13 July; however, the model produces too steep of a temperature decline. As the leading edge of the surge feature passes KB (0500–0600 UTC), the model produces too much surface cooling and MSLP rises earlier than observed, around 0400 UTC rather than 0500–0600 UTC. The pattern of a pressure jump followed by a brief plateau in the simulation (0400–1000 UTC) is real (0530–1200 UTC), but the significant pressure rise associated with the actual surge (0600–0900 UTC) is not modeled. It appears this second pressure rise may be related to the decaying convective complex very near KB between 0900–1200 UTC that is not in the control run. The elevated nighttime temperatures observed before 1200 UTC and the excess cooling from the simulation could also be explained by excessive radiational cooling in the model due to lack of cloud cover. The wind field of the model surge is too shallow by nearly 1000 m using the 10 m s^{-1} contour, less intense with maximum winds $\sim 7.5 \text{ m s}^{-1}$ less than observed, and an analysis period bias (RMSE) of -1.7 m s^{-1} (3.6 m s^{-1}), but has nearly correct timing (Figs. 11b,c). A lagged correlation finds the best agreement between the model wind profile and wind profiler observations that are lagged by 1 h.

At PP, the 2-m temperature and MSLP diurnal cycle is also represented well in the model, except for two notable dry air intrusions on 12 July seen in the dewpoint time series (Fig. 12a). This can be related back to excessive inflow of dry air from the Pacific Ocean in the NARR boundary conditions (Ciesielski and Johnson 2008).² There is an MSLP bias (RMSE) of 2.2 hPa (2.5 hPa), a temperature bias of -0.6 K (1.1 K), and a dewpoint bias of -1.3 K (3.4 K) at PP. The two convective outflow passages around 0000 and 0500 UTC are replicated in the simulation at around 0130 and 0500 UTC. The leading edge of the strong winds associated with the surge is timed well at PP (Figs. 12b,c), but again the surge is too shallow by nearly 1000 m and less intense with the maximum wind magnitude $7\text{--}9 \text{ m s}^{-1}$ less than reality with an analysis period bias (RMSE) of -1.1 m s^{-1} (3.7 m s^{-1}) at the profiler site. A lagged correlation finds the best agreement between the model wind profile and wind profiler observations that are lagged by 2.5 h.

It has been shown that the QNSE has a cool and moist bias of $1\text{--}2$ K in the 2-m temperature and dewpoint over the United States, especially in the late afternoon and evening (Wolff et al. 2011), which would explain the cool bias at KB and PP and the relatively good performance in dewpoint temperature. The NARR has a dry bias of -1.9 g kg^{-1} at the surface (about -1.5 -K dewpoint bias at a dewpoint of 298 K, MSLP of 1008 hPa; Ciesielski and Johnson 2008), while the KB and PP surface traces have dewpoint biases of -0.3 and 0.1 K (disregarding dry air intrusions from the Pacific Ocean on 12 July), respectively. This indicates the QNSE scheme biases improved the model dewpoints. Also, some of the differences between the observed and simulated surge depth may be related to the QNSE boundary layer scheme. A test run using the Yonsei University (YSU) planetary boundary layer scheme produces slightly warmer surface temperatures, a deeper boundary layer, and a deeper surge feature (not shown). This is expected due to the YSU scheme instantaneously mixing the entire boundary layer when activated (Weisman et al. 2008). In the QNSE run, the boundary layer was cooler, moister, and shallower, as expected. The YSU-simulated surge feature was too gravity current-like (abrupt, large surface temperature decline with largest wind speeds at leading edge), which does not match those observed as well as the QNSE run, thus it is not presented herein.

In regard to model convective evolution and precipitation coverage, the weaker convection, reduction of stratiform precipitation, and faster precipitation feature evolution are likely the primary reasons for a shallow and weak model surge. As highlighted above (Fig. 3), the simulation generally produces weaker convection and less stratiform precipitation in the convective cluster related to S1 and S2. Correspondingly, S1 and S2 are shallower and less intense than reality. Between 2200 UTC 12 July and around 0600 UTC 13 July, the model convective clusters along the SMO are slightly less intense, have less stratiform rain and evolve too quickly (Figs. 7 and 8). This would produce weaker convective outflow and cold pools just on the basis of a shorter duration of precipitation evaporating into the below-cloud layer. If modeled convective outflow is weaker than reality it may be expected that the surge would be weaker, as shown in the previous work (Stensrud et al. 1997) and in the results of the next section.

5. Microphysical and topographic modifications

In agreement with modeling (Stensrud et al. 1997) and observational (Hales 1972; Brenner 1974; RJ07) work, the control simulation shows convective outflow is likely a part of surge evolution. Also, inflow from the Pacific

² Ciesielski and Johnson (2008) show the NARR has an excessively strong GoC LLJ, which is related to strong flow from the Pacific Ocean into the northern GoC. This error will be in the simulation through the initial and boundary conditions.

Ocean may have played a role in initiating the surge and possibly modified its structure along the GoC. To investigate surge sensitivity to these two modulating processes, two modified runs were performed for the same time period as the control, 1200 UTC 11 July–0000 UTC 14 July. The first sensitivity experiment modifies the microphysics routine by removing all below-cloud rain evaporation, with the cloud base being defined as the first level above ground with a cloud water content greater than 0.1 g kg^{-1} . The goal of this experiment is to assess the impact of reduced rainwater evaporation on surge evolution. In the second sensitivity test, the peninsular ranges are raised to 1000 m from the tip of the peninsula to 32.5°N to reduce flow into the GoC from the Pacific Ocean. The goal of this experiment is to understand the role of gap flows in surge evolution. However, since there is only one run with each configuration, it is essentially impossible to assess the statistical significance of the differences.

a. No below-cloud evaporation

The control simulation shows that convective outflow may play a role in surge evolution. Removing below-cloud evaporation (No_SUBCLD run) may modify the outflow in a potentially significant manner. The evolution of convection on 12 and 13 July in this simulation is similar to the control run (Fig. 13), although the motion is slower than the control (not shown). The slower evolution and movement of convection in this experiment is expected because below-cloud evaporation has been removed, lessening the strength of cold pools (Benjamin 1968; Wakimoto 1982). For example, the convection in the northern GoC (near 30°N) is placed farther west in the control simulation and has a more extensive and slightly colder (on average) cold pool at 0000 UTC (Figs. 13a,b). In this case, the cold pool is defined by using the 306-K potential temperature contour as that is around 1–2 K cooler than the ambient air on the coastal plain. The minimum potential temperature north of 29°N in cold pools is 301 K on the first model level for both simulations; however, the surface area covered by potential temperatures less than 306 K is an order of magnitude larger in the control run with 2125 and 224 km^2 for the control and No_SUBCLD runs, respectively. Along the entirety of the SMO foothills, the No_SUBCLD run has an average temperature $\sim 1 \text{ K}$ higher in regions with potential temperatures less than 306 K on the first model surface above 200 m MSL.

Initially, the No_SUBCLD surge is more intense with a large area of enhanced moisture flux in the southern GoC (Fig. 14a), primarily due to slightly stronger inflow into the GoC from the south. The low-level pressure gradient is reduced in the control run by $\sim 10\%$ – 20%

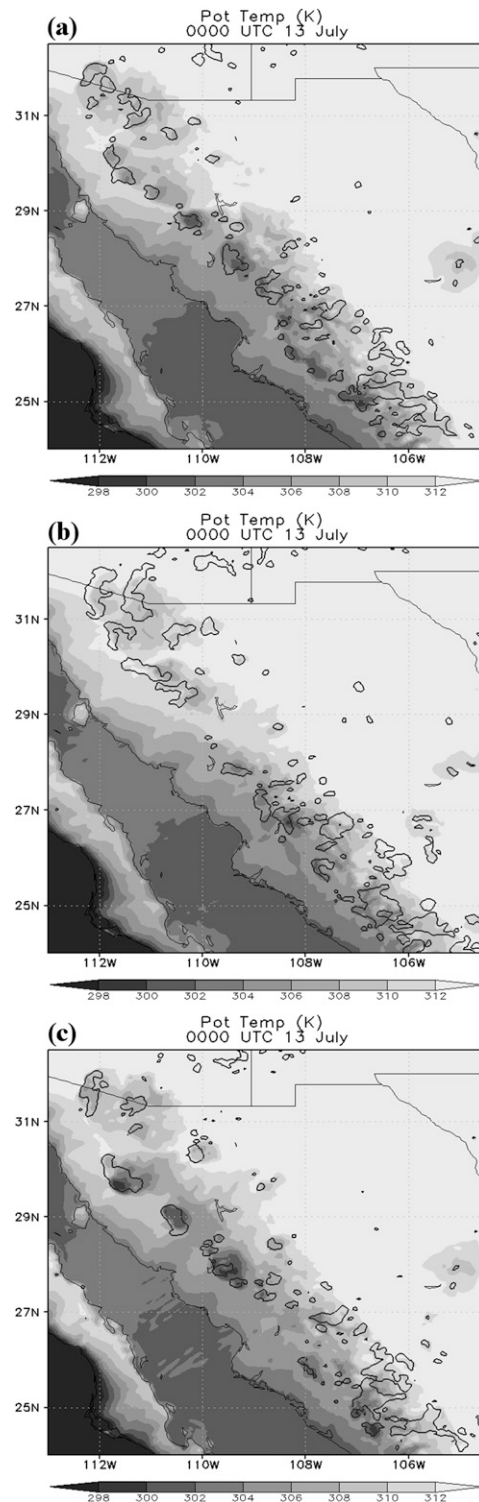


FIG. 13. First model level ($\sim 40 \text{ m}$ AGL) potential temperature (K) (shading) from (a) the control run and (b) No_SUBCLD at 0000 UTC 13 Jul. The 20-dBZ reflectivity contour (thick black) is given for reference.

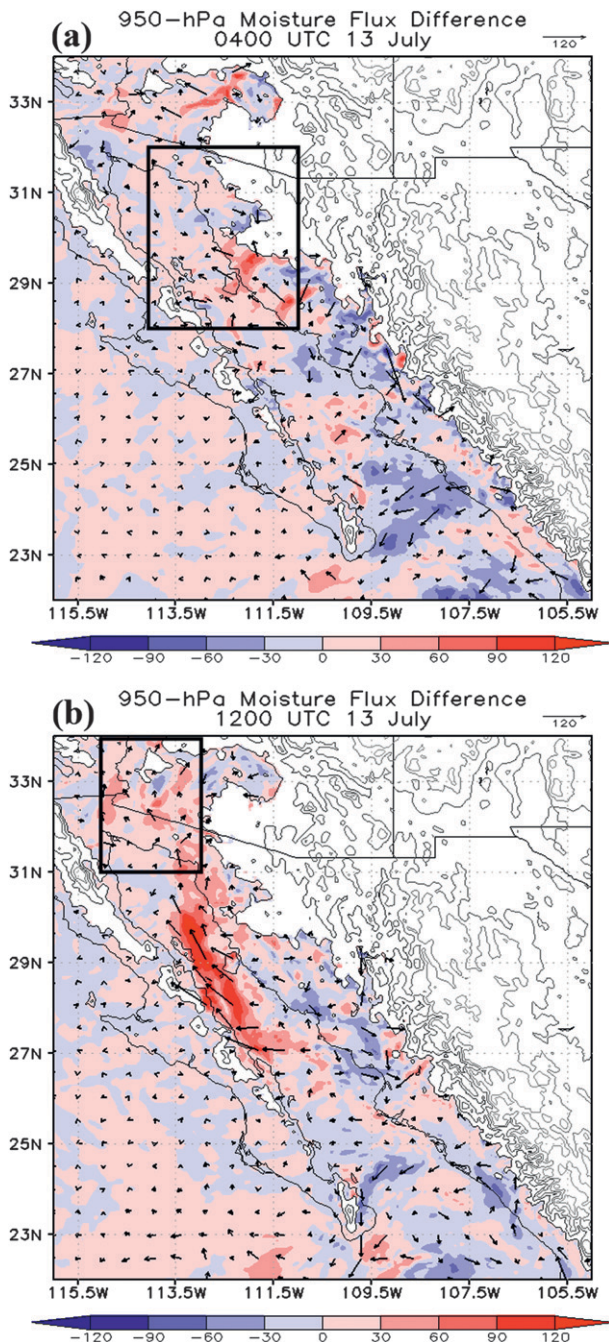


FIG. 14. Moisture flux differences (control – No_SUBCLD) at (a) 0400 and (b) 1200 UTC 13 Jul. In (a) the black box indicates the area used for the mean surge wind magnitude analysis, while in (b) the black box indicates the area used for the mean precipitable water analysis.

due to more extensive outflow (not shown). After the convective outflow impinges on the surge, the control run moisture flux is greater than the No_SUBCLD run along nearly the entire GoC (Fig. 14b). This is attributed to the lack of below-cloud evaporation in the

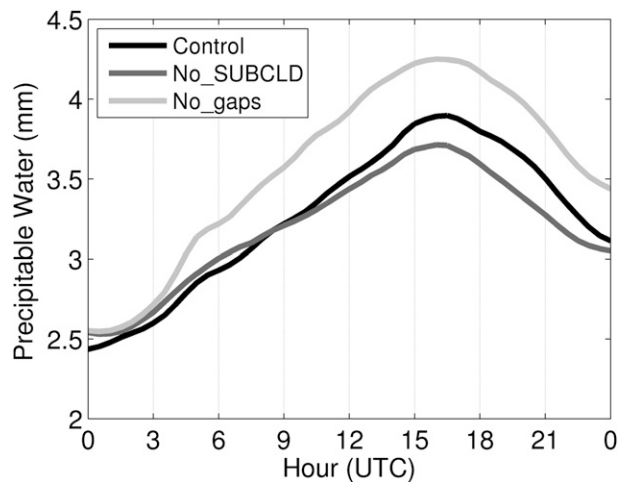


FIG. 15. Lowest 30 hPa above ground areal-average precipitable water in the extreme northern GoC and southern Arizona for 0000 UTC 13 Jul–0000 UTC 14 Jul.

No_SUBCLD simulation resulting in less convective outflow (Fig. 13). The mean magnitude of the wind field below 900 hPa in the northern GoC within the box shown in Fig. 14a is computed during the core of the surge (1000–1500 UTC 13 July) as another metric of surge intensity. The control simulation has a higher mean wind speed associated with the core of the surge event than the No_SUBCLD, 7.7 and 7.2 m s^{-1} respectively. A mean difference of 0.5 m s^{-1} over this large area and time period is notable. Finally, Fig. 15 displays the areal average precipitable water (PW) in extreme northern GoC/southern Arizona over the course of 13 July. Changes in PW correlate well with the net moisture flux at a point or over a region, thus it is a good indicator of the moistening ability of a surge event. Since surges are primarily low-level features, the PW from only the lowest 30 hPa is examined in an attempt to focus on surge-related moistening only. Figure 15 shows the control run has more net moisture flux into the extreme northern GoC, with the control run having an increase of $\sim 5\%$ over the No_SUBCLD run from 0000 UTC 13 July to 0000 UTC 14 July. These findings are all consistent with a stronger surge in the control run and agree with the results of Stensrud et al. (1997).

b. Modified topography

The control simulation indicates a possible role in surge formation and evolution for Pacific air intrusions into the GoC through gaps in the peninsular ranges. By raising the height of the topography to 1000 m, the amount of Pacific air entering the GoC is greatly reduced (not shown). Reduced Pacific inflow along the peninsular ranges creates an environment with more moisture in the lowest levels in the No_gaps run preceding

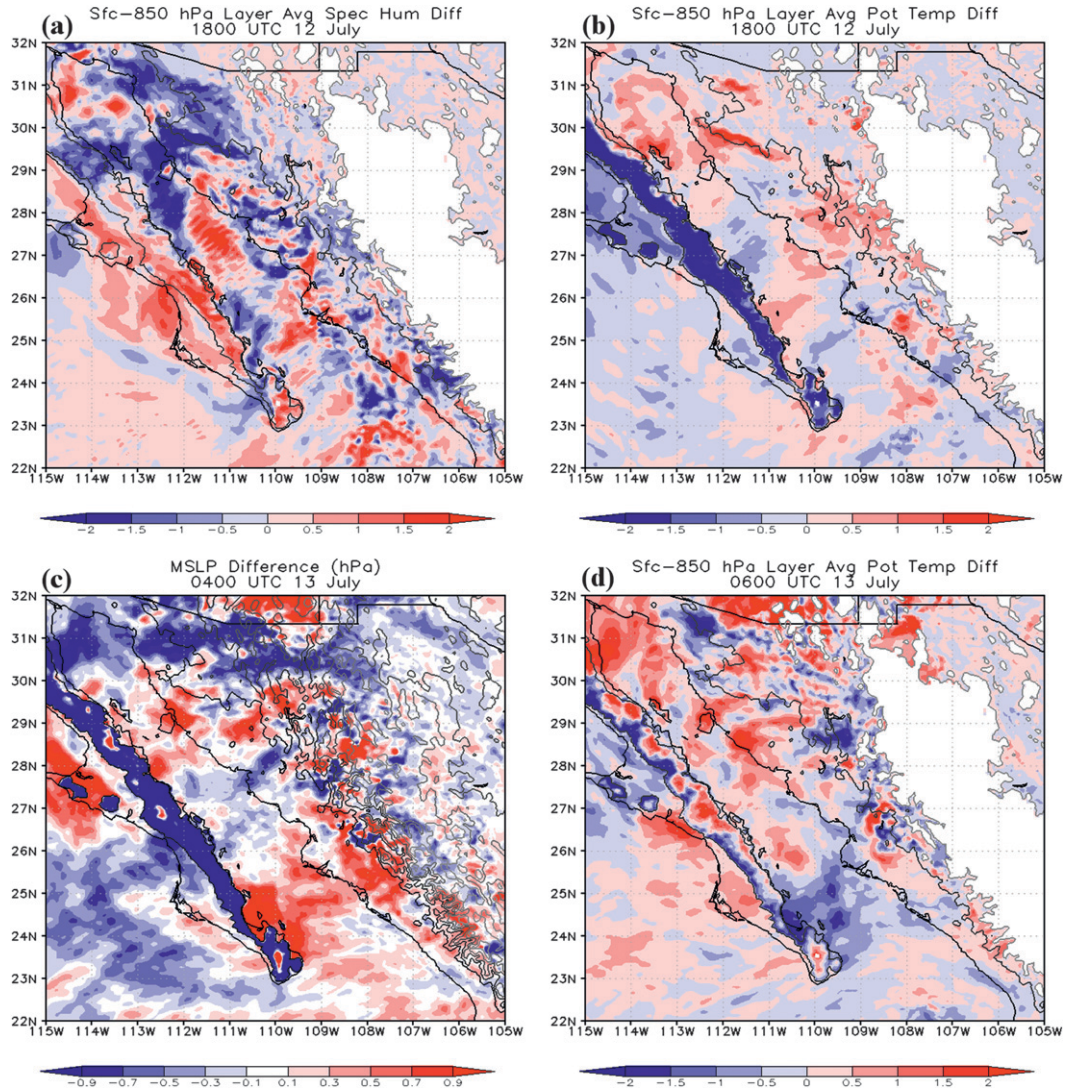


FIG. 16. Difference fields (control – No_gaps) of (a) surface to 850-hPa mass-weighted mean specific humidity (g kg^{-1}) at 1800 UTC 12 Jul, (b) potential temperature (K) at 1800 UTC 12 Jul, (c) mean sea level pressure at 0400 UTC 13 Jul, and (d) potential temperature (K) at 0600 UTC 13 Jul. Topography height (contours at 0, 500, and 1500 m with lighter shading indicating higher terrain), with areas in white above the 850-hPa elevation level.

convective initiation on the afternoon of 12 July. Nearly the entire northern coastal plain and SMO foothills (north of 29°N) have lower specific humidity in the control run (blue shading, Fig. 16a) and higher layer-average potential temperatures (red shading, Fig. 16b).

Higher layer-average potential temperatures in the control run seem counterintuitive since the Pacific air on the west side of the northern Baja is significantly colder than the air in the GoC (Fig. 17a). However, the peninsular ranges in the northern GoC provide just enough of a barrier to block the lowest levels, which creates a scenario where the air entering the gap regions has a higher potential temperature than the air in the GoC low-level mixed layer (Fig. 17a). Essentially it

blocks the air below the North Pacific marine inversion from entering the northern GoC. There is a well-mixed layer (the 310–312-K contours are relatively far apart) and hydraulic jump along the Baja Peninsula (114.5°W) in the control run (Fig. 17a), while the No_gaps run exhibits nearly completely blocked flow (Fig. 17b). The control simulation is also warmer and drier than the No_gaps simulation along the northeastern GoC coastal plain (Figs. 16a,b).

Where the real terrain is lower, near the mouth of the gulf, the gap flows entering the GoC are cooler than the gulf low-level mixed layer resulting in cooler layer-average potential temperatures in the control run near 24°N , 109.5°W (Figs. 16b,d). Therefore, it appears that

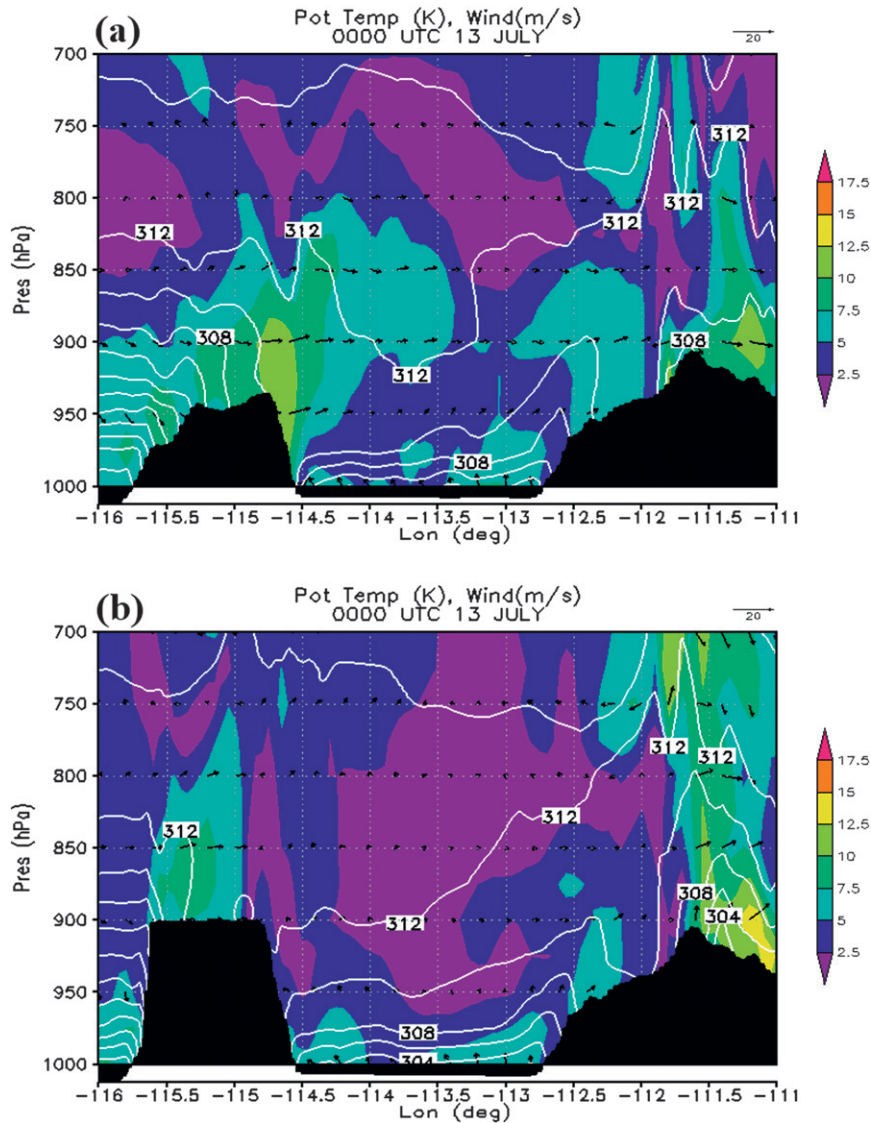


FIG. 17. As in Fig. 10c, but for a plane along 30°N for (a) the case study and (b) No_gaps simulations at 0000 UTC 13 Jul.

gap flow from the Pacific Ocean may not reinforce the low-level inversion in the northern GoC, but does so in the southern gulf. In the control simulation the flow is blocked along the northern Baja Peninsula in the lowest levels with any gap flows being potentially warmer than the mixed layer in the GoC resulting in a well-mixed warm area near the Baja Peninsula on the northwest side of the GoC (Figs. 16b,d and 17). Along the southern GoC the gaps are low enough to permit cooler Pacific air into the gulf.

The increased low-level moisture, along with higher CAPE (not shown), seems to be responsible for slightly more robust and long-lived convection in the No_gaps simulation, which generates larger cold pools (Fig. 13c). Using the 306-K contour as in section 5a, the No_gaps

simulation has a cold pool area along the SMO of $\sim 64\,000\text{ km}^2$ with an average and minimum temperature of 304.1 and 298 K, respectively, at 0000 UTC 13 July. That is compared to $59\,000\text{ km}^2$, 304.3 and 300 K for the control run at 0000 UTC 13 July. As shown in the No_SUBCLD run, weaker convective outflows have a negative impact on the surge strength in this case. This would imply a stronger surge event in the No_gaps simulation. Also, gravity wave phenomena, such as internal bores and Kelvin waves, require a stably stratified environment for propagation (Reason and Steyn 1992; Klemp et al. 1997). Higher layer-average potential temperatures in the control run over most of the GoC between 27° and 31°N (Fig. 16d) and a more neutral

lower atmosphere (Fig. 17), could weaken the surge in the control run.

All these factors should create a stronger surge in the No_gaps run, which is confirmed in Fig. 18, Fig. 15, and the average wind analysis. At 0400 UTC 13 July the No_gaps run has only slightly less moisture flux in the southern GoC (Fig. 18a). This result indicates the Pacific inflow noted in the control run is not a necessary factor in surge initiation. Instead, in the No_gaps simulation inflow from the mouth of the GoC is enhanced by $1\text{--}2\text{ m s}^{-1}$, relative to the control simulation. Again, this is caused by a reduced low-level pressure gradient in the control simulation. However, in this case the gap flows north of the tip of the GoC and convective placement in the control simulation combine to create the higher surface pressures north of the GoC entrance (Fig. 16c), via more cool air north of the GoC entrance, which reduce inflow into the GoC. The No_gaps simulation moisture flux is significantly enhanced relative to the control simulation after convective outflow interaction (Fig. 18b). This behavior is again due to the reduction of gap flows from the Pacific and the stronger convective outflows present in the No_gaps simulation. The average wind magnitude analysis finds magnitudes for the core surge time period of 7.7 and 8.3 m s^{-1} for the control and No_gaps runs, respectively. Finally, Fig. 15 shows the No_gaps run has a larger PW increase in the extreme northern GoC than the control run. This discussion shows that the basic nature and occurrence of the surge event are not altered in a qualitative way in the No_gaps run; however, there is an enhancement in the surge intensity and moisture transport.

6. Summary and discussion

A convection-permitting simulation over the entire core of the North American monsoon (NAM) using the WRF-ARW model for the 12–14 July 2004 Gulf of California (GoC) southerly moisture surge is able to reproduce the observed precursor and initial surge event on 12 and 13 July, respectively. It captures the general timing and features of convection in the southern GoC on 12 July along with a corresponding cold pool and a deeper disturbance in the flow field, denoted as structure 2 (S2) in both Mejia et al. (2010) and in this paper, which may contribute to or modify the initiation of the surge on 13 July. While this feature is not the actual surge, it is important because it signifies the leading edge of southerly flow, slight cooling and moistening below 800 hPa in the southern and central GoC with the southerly flow continuing through the surge on 13 July. Thus, S2 appears to precondition the southern and central GoC to a cooler and moister state leading into the surge event.

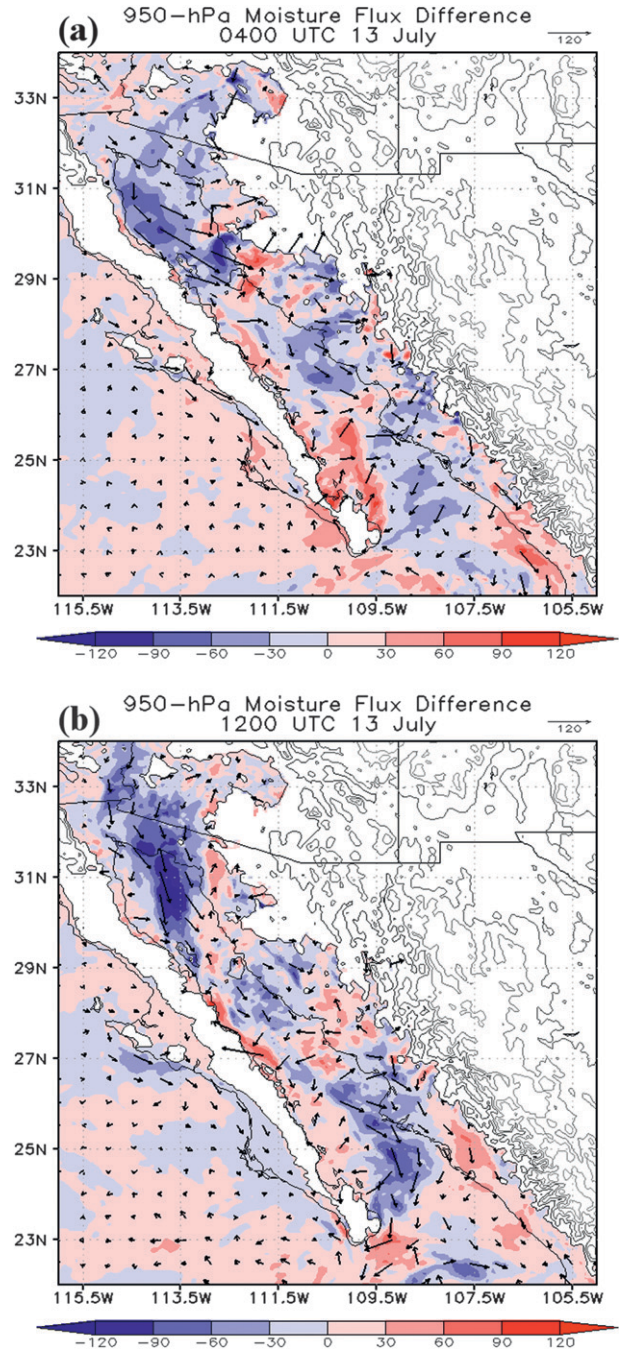


FIG. 18. Moisture flux differences (control – No_gaps) for the same times as in Fig. 14.

On 13 July the simulation correctly reproduces convection along the Sierra Madre Occidental (SMO) that propagates off the SMO toward the GoC through around 0900 UTC, but it produces too little stratiform precipitation and evolves the convection too quickly as compared to the radar network observations. The timing

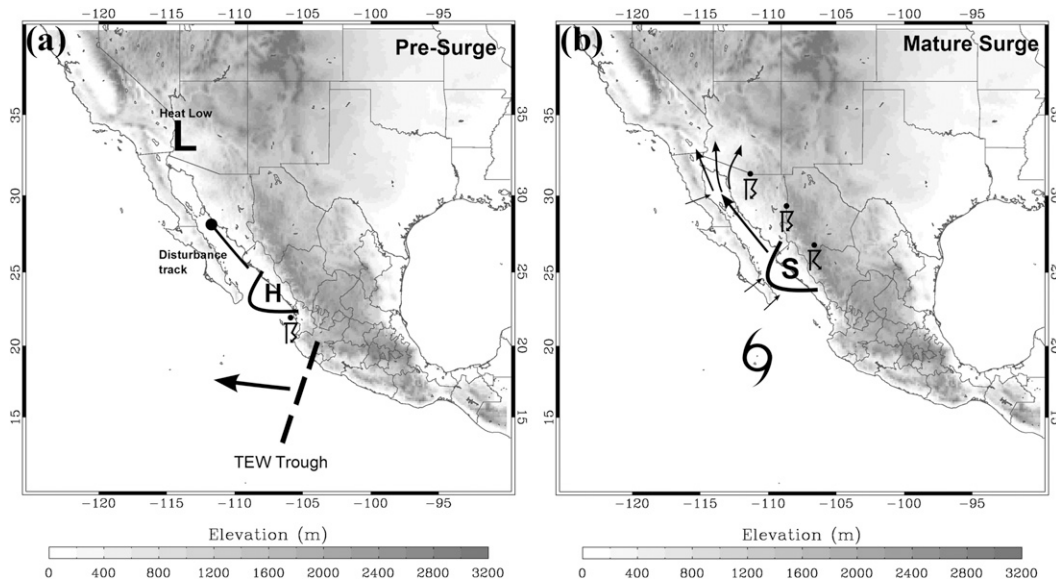


FIG. 19. General schematic depiction of the evolution of important features on 12–13 Jul. (a) The black H and curved line denote the position of the coastally trapped disturbance (S2) and corresponding higher MSLP around 1200 UTC with the straight line ending near 28°N indicating motion and dissipation location, the heavy thunderstorm symbol denotes the location of the organized convective cluster around 0900 UTC, while the dashed line and arrow give the location and movement of the TEW trough. (b) The S, curve, and thick arrow denote the general initiation location of the gulf surge as well as its motion, while the three thinner arrows denote the surge spreading into the northern GoC and desert Southwest after 1200 UTC. The smallest arrows indicate general areas of gap/inflow from Pacific Ocean before 1200 UTC. The tropical cyclone symbol denotes the location of Tropical Storm Blas around 1200 UTC 13 Jul. The heavy thunderstorm symbols denote areas of more organized and persistent convection between 0000–1000 UTC, while the moderate thunderstorm symbol (near 25°N) indicates less organized and persistent convection.

of the surge feature at Kino Bay (KB) and Puerto Penasco (PP) is slightly advanced in the simulation, by 1–3 h. Surface time series show that the simulation generally reproduces the correct surface features, but the simulated surge is too shallow and has weaker wind speeds than observed. This may be related to the boundary layer scheme in the model, or be due to the lack of stratiform precipitation and corresponding weaker convective outflows impacting surge strength, or both. However, the simulated surge structure in a cross-gulf cross section agrees very well with that observed by the NOAA WP-3D, with the wind field in this case only slightly shallower than observed. The simulated surge has a total system speed of $\sim 22 \text{ m s}^{-1}$ and slows when entering the northern GoC, which is in very good agreement with the average observed surge system speed ($\sim 17\text{--}25 \text{ m s}^{-1}$) and evolution diagnosed by RJ07.

Figure 19 shows the general evolution of the simulated surge on 12 and 13 July, respectively. Initially, convection associated with the tropical easterly wave precursor to Tropical Storm Blas creates a gravity wave (structure 1, S1) in the southern GoC on 12 July around 0600–0900 UTC. This gravity wave generates another impulse (structure 2, S2), with an associated surface high pressure, that propagates up the GoC and becomes

diffuse just south of KB around 2200 UTC 12 July. Southerly flow and slight cooling and moistening below $\sim 800 \text{ hPa}$ in the observations and $\sim 750 \text{ hPa}$ in the simulation are seen behind S2. Convection then forms along the length of the SMO late on 12 July into 13 July. Inflow from the mouth of the GoC and Pacific Ocean along with convective outflow impinging on the southern GoC appears to initiate the primary surge event by early on 13 July. Continued convective outflow entering the GoC intensifies the surge as it propagates up the GoC. Substantial low-level cooling and moistening are associated with the simulated surge as the core reaches the northern GoC.

Stensrud et al. (1997), Fuller and Stensrud (2000), and Adams and Stensrud (2007) show that gulf surges are typically preceded by tropical easterly wave passage. Adams and Stensrud (2007) also find that removal of tropical easterly waves in simulations results in weaker surges that occur at different times and are often associated with waves generated internally by the model. In this case, the surge signal seen at PP around 1200 UTC 13 July is preceded by the disturbance on 12 July associated with a tropical easterly wave, which could possibly explain how TEW/TCs are tied to gulf surge events. Removal of the preceding feature on 12 July may change

the evolution and character of the surge event on 13 July since S2 is followed by cooling, moistening, and southerly flow in the southern and central GoC that extends through 13 July. It could be that without this initial cooling and inflow into the southern GoC, the surge evolution along the southern SMO would be different. This possibility should be the subject of further study.

To isolate processes generating and sustaining the surge event, two sensitivity experiments were performed. The first sensitivity test involved removing evaporation from rain below the cloud base (No_SUBCLD) and shows that the moisture flux and mean wind speed in the northern GoC during the peak hours of the surge, 1000–1500 UTC 13 July, is lessened as compared to the control simulation. These findings agree with Stensrud et al. (1997) where a run without any diabatic processes developed a much weaker surge compared to their control run. This simulation produces a weaker surge with less drastic model modifications and at a convection-permitting resolution. The second sensitivity simulation examines the influence of gap flow (No_gaps) on surge evolution and strength by increasing the height of the peninsular ranges so that flow is nearly entirely blocked from entering the GoC from the Pacific Ocean. The No_gaps simulation has slightly more moisture with more extensive convection near the SMO that produces more convective outflow and a resulting increase in surge intensity as compared to the control simulation. Most importantly, the No_gaps simulation shows that the general features and evolution of the surge are similar regardless of the topography of the Baja Peninsula.

Acknowledgments. The authors thank Paul Ciesielski, Brian McNoldy, Rick Taft, and Sue van den Heever for all their assistance relating to this research, as well as three anonymous reviewers and Editor David Schultz for their helpful comments. This work was supported by NASA Headquarters under NASA Contracts NNX07AD35G, NNX10AG81G, and by the National Science Foundation, Mesoscale Dynamic Meteorology and Physical and Dynamic Meteorology Programs, under Grants ATM-0639461 and AGS-0966758. Also, we would like to acknowledge the high-performance computing support provided by NCAR's Computational and Information Systems Laboratory, which is sponsored by the National Science Foundation.

REFERENCES

- Adams, D. K., and A. C. Comrie, 1997: The North American monsoon. *Bull. Amer. Meteor. Soc.*, **78**, 2197–2213.
- Adams, J. L., and D. J. Stensrud, 2007: Impact of tropical easterly waves on the North American monsoon. *J. Climate*, **20**, 1219–1238.
- Anderson, B. T., J. O. Roads, and S.-C. Chen, 2000a: Large-scale forcing of summertime monsoon surges over the Gulf of California and the southwestern United States. *J. Geophys. Res.*, **105** (D19), 24 455–24 467.
- , —, and —, 2000b: Regional simulation of the low-level monsoon winds over the Gulf of California and southwestern United States. *J. Geophys. Res.*, **105** (D14), 17 955–17 969.
- , —, and —, 2001: Model dynamics of summertime low-level jets over northwestern Mexico. *J. Geophys. Res.*, **106** (D4), 3401–3413.
- Badan-Dangon, A., C. E. Dorman, M. A. Merrifield, and C. D. Winant, 1991: The lower atmosphere over the Gulf of California. *J. Geophys. Res.*, **96** (C9), 16 877–16 896.
- Barthlott, C., J. W. Schipper, N. Kalthoff, B. Adler, C. Kottmeier, A. Blyth, and S. Mobbs, 2010: Model representation of boundary-layer convergence triggering deep convection over complex terrain: A case study from COPS. *Atmos. Res.*, **95**, 172–185.
- Benjamin, T. B., 1968: Gravity currents and related phenomena. *J. Fluid Mech.*, **31**, 209–248.
- Berberly, E. H., 2001: Mesoscale moisture analysis of the North American monsoon. *J. Climate*, **14**, 121–137.
- Bordoni, S., and B. Stevens, 2006: Principal component analysis of the summertime winds over the Gulf of California: A gulf surge index. *Mon. Wea. Rev.*, **134**, 3395–3414.
- , P. E. Ciesielski, R. H. Johnson, B. D. McNoldy, and B. Stevens, 2004: The low-level circulation of the North American monsoon as revealed by QuikSCAT. *Geophys. Res. Lett.*, **31**, L10109, doi:10.1029/2004GL020009.
- Brenner, I. S., 1974: A surge of maritime tropical air—Gulf of California to the southwestern United States. *Mon. Wea. Rev.*, **102**, 375–389.
- Bryan, G. H., and H. Morrison, 2012: Sensitivity of a simulated squall line to horizontal resolution and parameterization of microphysics. *Mon. Wea. Rev.*, **140**, 202–225.
- , J. C. Wyngaard, and J. M. Fritsch, 2003: Resolution requirements for the simulation of deep moist convection. *Mon. Wea. Rev.*, **131**, 2394–2416.
- Carleton, A. M., D. A. Carpenter, and P. J. Weser, 1990: Mechanisms of interannual variability of southwest United States summer precipitation maximum. *J. Climate*, **3**, 999–1015.
- Ciesielski, P. E., and R. H. Johnson, 2008: Diurnal cycle of surface flows during 2004 NAME and comparison to model reanalysis. *J. Climate*, **21**, 3890–3913.
- Douglas, A. V., and P. J. Englehart, 2007: A climatological perspective of transient synoptic features during NAME 2004. *J. Climate*, **20**, 1947–1954.
- Douglas, M. W., 1995: The summertime low-level jet over the Gulf of California. *Mon. Wea. Rev.*, **123**, 2334–2347.
- , and J. C. Leal, 2003: Summertime surges over the Gulf of California: Aspects of their climatology, mean structure, and evolution from radiosonde, NCEP reanalysis, and rainfall data. *Wea. Forecasting*, **18**, 55–74.
- , R. A. Maddox, K. Howard, and S. Reyes, 1993: The Mexican monsoon. *J. Climate*, **6**, 1665–1677.
- , A. Valdez-Manzanilla, and R. G. Cueto, 1998: Diurnal variation and horizontal extent of the low-level jet over the northern Gulf of California. *Mon. Wea. Rev.*, **126**, 2017–2025.
- Fuller, R. D., and D. J. Stensrud, 2000: The relationship between tropical easterly waves and surges over the Gulf of California during the North American monsoon. *Mon. Wea. Rev.*, **128**, 2983–2989.

- Gilmore, M. S., J. M. Straka, and E. N. Rasmussen, 2004: Precipitation and evolution sensitivity in simulated deep convective storms: Comparisons between liquid-only and simple ice and liquid phase microphysics. *Mon. Wea. Rev.*, **132**, 1897–1916.
- Gochis, D. J., A. J. Jimenez, C. J. Watts, J. Garatuza-Payan, and W. J. Shuttleworth, 2004: Analysis of 2002 and 2003 warm season precipitation from the North American Monsoon Experiment event rain gauge network. *Mon. Wea. Rev.*, **132**, 2938–2953.
- Haertel, P. T., R. H. Johnson, and S. N. Tulich, 2001: Some simple simulations of thunderstorm outflows. *J. Atmos. Sci.*, **58**, 504–516.
- Hales, J. E., Jr., 1972: Surges of maritime tropical air northward over the Gulf of California. *Mon. Wea. Rev.*, **100**, 298–306.
- Higgins, R. W., and W. Shi, 2005: Relationships between Gulf of California moisture surges and tropical cyclones in the eastern Pacific basin. *J. Climate*, **18**, 4601–4620.
- , —, and C. Hain, 2004: Relationships between Gulf of California moisture surges and precipitation in the southwestern United States. *J. Climate*, **17**, 2983–2997.
- , and Coauthors, 2006: The NAME 2004 field campaign and modeling strategy. *Bull. Amer. Meteor. Soc.*, **87**, 79–94.
- Johnson, R. H., P. E. Ciesielski, B. D. McNoldy, P. J. Rogers, and R. K. Taft, 2007: Multiscale variability of the flow during the North American Monsoon Experiment. *J. Climate*, **20**, 1628–1648.
- Jones, D. M. A., 1956: Rainfall drop size-distribution and radar reflectivity. Research Rep. 6, Illinois State Water Survey Meteorological Laboratory, University of Illinois, Urbana, IL, 39 pp. [Available from the Illinois State Water Survey Meteorological Laboratory, University of Illinois, Urbana, IL 61820.]
- Klemp, J. B., R. Rotunno, and W. C. Skamarock, 1997: On the propagation of internal bores. *J. Fluid Mech.*, **331**, 81–106.
- Knupp, K., 2006: Observational analysis of a gust front to bore to solitary wave transition within an evolving nocturnal boundary layer. *J. Atmos. Sci.*, **63**, 2016–2035.
- Lang, T. L., D. A. Ahijevch, S. W. Nesbitt, R. E. Carbone, S. A. Rutledge, and R. Cifelli, 2007: Radar-observed characteristics of precipitating systems during NAME 2004. *J. Climate*, **20**, 1713–1733.
- Li, J., S. Sorooshian, W. Higgins, X. Gao, B. Imam, and K. Hsu, 2008: Influence of spatial resolution on diurnal variability during the North American monsoon. *J. Climate*, **21**, 3967–3988.
- Maddox, R. A., D. M. McCollum, and K. W. Howard, 1995: Large-scale patterns associated with severe summertime thunderstorms over central Arizona. *Wea. Forecasting*, **10**, 763–778.
- Marshall, J. S., and W. Mc K. Palmer, 1948: The distribution of raindrops with size. *J. Meteor.*, **5**, 165–166.
- Martin, E. R., and R. H. Johnson, 2008: An observational and modeling study of an atmospheric internal bore during NAME 2004. *Mon. Wea. Rev.*, **136**, 4150–4167.
- Mejia, J. F., and M. W. Douglas, 2005: Mean structure and variability of the low-level jet across the central Gulf of California from NOAA WP-3D flight level observations during the North American Monsoon Experiment. Preprints, *Sixth Conf. on Coastal Atmospheric and Oceanic Prediction and Processes*, San Diego, CA, Amer. Meteor. Soc., 5.8. [Available online at http://ams.confex.com/ams/Annual2005/techprogram/paper_86861.htm.]
- , —, and P. J. Lamb, 2010: Aircraft observations of the 12–15 July 2004 moisture surge event during the North American Monsoon Experiment. *Mon. Wea. Rev.*, **138**, 3498–3513.
- Mesinger, F., and Coauthors, 2006: North American Regional Reanalysis. *Bull. Amer. Meteor. Soc.*, **87**, 343–360.
- Pielke, R. A., Sr., 2002: *Mesoscale Meteorological Modeling*. 2nd ed. International Geophysical Series, Vol. 78, Academic Press, 676 pp.
- Reason, C. J. C., and D. G. Steyn, 1992: The dynamics of coastally trapped ridges in the lower atmosphere. *J. Atmos. Sci.*, **49**, 1677–1692.
- Rogers, P. J., and R. H. Johnson, 2007: Analysis of the 13–14 July gulf surge event during the 2004 North American Monsoon Experiment. *Mon. Wea. Rev.*, **135**, 3098–3117.
- Rotunno, R., J. B. Klemp, and M. L. Weisman, 1988: A theory for strong, long-lived squall lines. *J. Atmos. Sci.*, **45**, 463–485.
- Simpson, J. E., 1982: Gravity currents in the laboratory, atmosphere, and ocean. *Annu. Rev. Fluid Mech.*, **14**, 213–234.
- , 1997: *Gravity Currents in the Environment and the Laboratory*. Cambridge University Press, 244 pp.
- Stensrud, D. J., 2007: *Parameterization Schemes: Keys to Understanding Numerical Weather Prediction Models*. Cambridge University Press, 478 pp.
- , R. L. Gall, S. L. Mullen, and K. W. Howard, 1995: Model climatology of the Mexican monsoon. *J. Climate*, **8**, 1775–1793.
- , —, and M. K. Nordquist, 1997: Surges over the Gulf of California during the Mexican monsoon. *Mon. Wea. Rev.*, **125**, 417–437.
- Thompson, G., P. R. Field, R. M. Rasmussen, and W. D. Hall, 2008: Explicit forecasts of winter precipitation using an improved bulk microphysics scheme. Part II: Implementation of a new snow parameterization. *Mon. Wea. Rev.*, **136**, 5095–5115.
- Trier, S. B., J. H. Marsham, C. A. Davis, and D. A. Ahijevych, 2011: Numerical simulations of the postsunrise reorganization of a nocturnal mesoscale convective system during 13 June IHOP_2002. *J. Atmos. Sci.*, **68**, 2988–3011.
- Vera, C., and Coauthors, 2006: Toward a unified view of the American monsoon systems. *J. Climate*, **19**, 4977–5000.
- Wakimoto, R. M., 1982: The life cycle of thunderstorm gust fronts as viewed with Doppler radar and rawinsonde data. *Mon. Wea. Rev.*, **110**, 1060–1082.
- Warner, J., 1969: The microstructure of cumulus cloud. Part I: General features of the droplet spectrum. *J. Atmos. Sci.*, **26**, 1049–1059.
- Warner, T. T., 2011: *Numerical Weather and Climate Prediction*. Cambridge University Press, 548 pp.
- Weisman, M. L., C. Davis, W. Wang, K. W. Manning, and J. B. Klemp, 2008: Experiences with 0–36-h explicit convective forecasts with the WRF-ARW model. *Wea. Forecasting*, **23**, 407–437.
- Wolff, J., L. Nance, J. H. Gotway, P. Oldenburg, M. Harrold, and Z. Trabold, 2011: WRF QNSE test and evaluation. Preprints, *20th Conf. on Numerical Weather Prediction*, Seattle, WA, Amer. Meteor. Soc., P470. [Available online at <http://ams.confex.com/ams/91Annual/webprogram/Paper180881.html>.]